ANALYTICAL SOLUTIONS FOR BLOCH WAVES IN RESONANT PHONONIC CRYSTALS: DEEP-SUBWAVELENGTH ENERGY SPLITTING AND MODE STEERING BETWEEN TOPOLOGICALLY PROTECTED INTERFACIAL AND EDGE STATES

by R. WILTSHAW[†]

(*Department of Mathematics, Imperial College London, London SW7 2AZ, UK*)

J. M. DE PONTI

(*Department of Civil and Environmental Engineering, Politecnico di Milano, Piazza Leonardo da Vinci, 32, 20133 Milano, Italy*)

R. V. CRASTER

(*Department of Mathematics, Imperial College London, London SW7 2AZ, UK*)

[Received 7 October 2022. Revised 21 February 2023. Accepted 27 February 2023]

Summary

We derive analytical solutions based on singular Green's functions, which enable efficient computations of scattering simulations or Floquet–Bloch dispersion relations for waves propagating through an elastic plate, whose surface is patterned by periodic arrays of elastic beams. Our methodology is versatile and allows us to solve a range of problems regarding arrangements of multiple beams per primitive cell, over Bragg to deep-subwavelength scales; we cross-verify against finite element numerical simulations to gain further confidence in our approach, which relies upon the hypothesis of Euler–Bernoulli beam theory considerably simplifying continuity conditions such that each beam can be replaced by point forces and moments applied to the neutral plane of the plate. The representations of Green's functions by Fourier series or Fourier transforms readily follows, yielding rapid and accurate analytical schemes. The accuracy and flexibility of our solutions are demonstrated by engineering topologically non-trivial states, from primitive cells with broken spatial symmetries, following the phononic analogue of the Quantum Valley Hall Effect. Topologically protected states are produced and coexist along: interfaces between adjoining chiral-mirrored bulk media, and edges between one such chiral bulk and the surrounding bare elastic plate, allowing topological circuits to be designed with robust waveguiding. Our topologically protected interfacial states correspond to zero-line modes, and our topological edgestates are produced in accordance with the bulk-edge correspondence. These topologically non-trivial states exist within near flexural resonances of the constituent beams of the phononic crystal and hence can be tuned into a deep-subwavelength regime.

1. Introduction

Identifying degeneracies, such as locally dispersionless band structures meeting at a point, allows periodic structured media to be constructed with remarkable propagation properties, for example,

[†]Corresponding author <r.wiltshaw17@imperial.ac.uk>

Q. Jl Mech. Appl. Math, Vol. 76. No. 2 © The Author, 2023. Published by Oxford University Press.

Advance Access publication 7 April 2023. https://doi.org/10.1093/qjmam/hbad001

extraordinary transmission (**1**–**3**), cloaking (**4**, **5**), interfacial states (**6**–**23**, **67**), edge states (**24**–**26**), one-way propagation (**24**, **27**–**31**) or a near-zero refractive index (**4**)—all of which can be engineered in a variety of physical settings. This has led to extremely active communities, predominantly in photonics (**32**, **33**) and phononics (**34**, **35**), extensively researching designs and devices that take advantage of this power to manipulate waves.

The characteristic length scale of fundamental units forming a crystalline media can have a variety of scales depending on the frequencies of propagating waves to be controlled. Optical properties of nanomaterials/nanocomposites, for example, the lustre attained by potteries and glasses (**36**) can be explained through a modern photonic crystal framework. Nature provides examples ranging from microphotonic crystals forming the iridescent colours of opals and certain butterfly species (**37**), to geophysical scales where forests have been shown to act as phononic crystals capable of controlling seismic waves (**38**, **39**) by manipulating surface Rayleigh waves via subwavelength band gaps. The focus of (**38**) was on compressional resonances of trees of $\mathcal{O}(10)$ Hz, providing strong attenuation of waves with wavelengths 5–10 times that of the lattice spacing of the forest.

Herein, we design phononic crystals formed from periodic arrays of Euler–Bernoulli beams atop a thin elastic plate. We consider topological arrangements of beams within the cell that repeats, and demonstrate the existence of symmetry protected Dirac cones which coincide with the flexural resonances of the beams; these degeneracies, once gapped, produce very low $\mathcal{O}(0.1)$ Hz frequency band gaps allowing the manipulation of waves whose wavelengths are 35–40 times that of the lattice spacing. Our designs produce topologically non-trivial states which are capable of confining modes along various interfaces and edges, following the phononic analogue of the QVHE. The topological protection produced by our designs show a variety of conventional and new properties at the deep-subwavelength scale.

The valleytronics community (**6**–**23**, **67**) often use the terms interfacial and edge states interchangeably. For clarity, we will refer to states existing along the interface between two chiral-mirrored bulk media as interfacial states. The states which live on the edge of the crystal, between the bulk derived from one such chiral pair and the free space, will be referred to as edge states. We demonstrate how these topologically protected interfacial and edge states co-exist within the subwavelength band gap of the underlying bulk media, and how modal conversion or preservation allows modes to efficiently navigate corners or split energy between the interfaces and edges of our phononic crystal designs—as shown later in Figs 9, 13 and 14. The near-resonant behaviour of our topologically distinct valleys allows us to tune our topologically protected states into a deep-subwavelength regime, where we demonstrate the interfacial and edge modes are sufficiently robust to navigate gentle and sharp (**40**) corners, with minimal backscatter, due to the combination of low-frequency resonances (**25**, **41**) and topological protection (**24**, **42**); our edgemodes either propagate around the entire perimeter of the crystal, or hybridise into corner states (**43**–**45**) which readily shed energy into the surrounding free space.

Recent years have witnessed an increasing popularity of metamaterial concepts, based on local resonance phenomenon, to control the propagation of electromagnetic (**46**), acoustic (**35**, **47**) and elastic waves (**48**) in artificially engineered media. In elasticity, resonant structures formed from arrays of beams yield superior characteristics for broadband wave focusing (**49**), mode conversion (**50**–**52**) and energy harvesting (**53**–**55**). Novel works combining resonance and topological protection (**41**, **56**–**63**) achieve confinement of modes at the subwavelength scale—for instance, (**41**, **56**–**63**) consider zero-line modes, the robustness of which is demonstrated by introducing bends (**8**, **9**, **13**, **15**, **17**, **22**, **42**, **64**–**66**) or splitting energy (**68**–**70**).

In a phononic setting, long waves can have negative impacts; for example, those who live in flats or in close proximity to large scale transport infrastructure will often complain of long-wave disturbances, generated from low-frequency changes to pressure (for example, music with deep bass) or vibrations from passing vehicles. Long-wave disturbances also have the potential to be highly damaging. Naturally occurring seismic events are well known to cause large scale, irreparable damage to sensitive infrastructure; for example, earthquakes whose epicentre could be considered far field (**50**, **71**) are of particular concern to densely populated urban environments. There is considerable research around mechanisms and devices for low-frequency long waves to be manipulated and steered, with resonant phononic crystals showing great promise in areas of seismic and phononic passive protection.

The extraordinary properties exhibited by our phononic crystal designs require symmetry-based arguments following the approach of valleytronics (**6**, **72**–**75**). We design our media through Floquet–Bloch (**76**, **77**) analysis, allowing the dispersion relation of doubly periodic structured medium to be deduced from eigensolutions through primitive cells with Floquet–Bloch boundary conditions. Once the underlying structure has been suitably engineered, we test the localisation of our topologically non-trivial states by considering: eigenproblems formed from supercells (**8**) of these fundamental units, or scattering simulations of large finite collections of these cells. These problems can be solved by general finite element method (FEM) analysis; however, when considering arrays of beams attached to plates, the number of nodes required to discretise the problem leads to computationally expensive results with long computation times. Nevertheless, FEM analysis leads to accurate results and is by far the most popular method considered by the meta-material community.

We aim to develop much faster and efficient methods based on singular Green's functions. Our solutions are cross-verified against FEM computations and are shown to be highly accurate, efficient and flexible enough to consider a variety of Floquet–Bloch eigensolutions and scattering simulations. Codes based on these analytical solutions are fast to run, thereby expediting the process of modifying the underlying media to produce the required dispersion. Moreover, once the crystal has been designed, we need to test its effectiveness in achieving the desired effect through direct scattering simulations of finite arrangements of scatterers under incidence. Analytically considering scatterers placed in fields with infinite domains allows for efficient computations. For instance, the scattering simulations in Figs 9, 13 and 14 are merely plots of our analytical solutions; not only do they contain $\mathcal{O}(10^4)$ beams judiciously placed atop the elastic plate, each beam scatters the field such that the Sommerfeld radiation condition is satisfied at infinity. Moreover, each computation took $\mathcal{O}(10)$ minutes for a single frequency, even near resonance. Perfectly matched layers can be used within FEM computations to replicate these infinite domains and perform similar scattering simulations; however, the computational time and power required for such results would be considerably larger than our analysis.

The aims of this study are to outline all necessary analytical nuances to deal with singular Green's functions, allowing simple codes to be constructed such that Floquet–Bloch eigensolutions or scattering simulations can be computed for phononic crystals built from arrangements of objects that can resonate. In section 2, we derive the singular Green's functions for one beam atop an elastic plate of infinite expanse; we extend this solution to consider dispersion relations and eigenmodes for Floquet–Bloch wave propagation through periodic infinite arrays of beams atop a plate in section 3, and scattering simulations for finite collections of beams atop an elastic plate under incident forcing in section 4. The solutions of these problems are determined either by solving an algebraic eigenvalue problem, or by computing the inverse of a matrix. We test our analytical solutions against FEM computations in section 5. Finally in section 6, we demonstrate the simplicity,

accuracy and efficiency of our analytically constructed codes by designing a variety of topologically protected states, existing within deep-subwavelength topological band gaps of the underlying bulk medium. We also test these designs by performing large scale scattering simulations in which our phononic crystals, formed by finite arrays of these primitive cells, are subject to scattering from some incident source of energy.

2. Singular Green's functions in elasticity

Consider a thin elastic plate of infinite extent, whose surface is patterned by some doubly periodic arrangement of beams as shown in Fig. 1. The beams considered are of circular cross-section, centred in the $x - y$ plane on $\mathbf{x} = \mathbf{X}$ and of radius $r = \epsilon$, where we define the radial position $r = |\mathbf{x} - \mathbf{X}|$.

The Green's functions, whilst providing flexible, efficient and accurate results are not simple to utilise—they contain trigonometric and hyperbolic functions (**78**) of frequency and singularities (**42**, **79**–**82**) as one approaches the centre of a scatterer. Through careful consideration, the singularities present within Green's functions can be removed allowing semi-analytical computations to follow; direct scattering simulations utilising generalised Foldy's method (**42**, **83**–**85**) remove such singularities by examining inner limits of the external field for every scatterer. Moreover, conditionally convergent Fourier series can be rearranged in a novel way such that singularities present in the field naturally cancel from the problem (**85**).

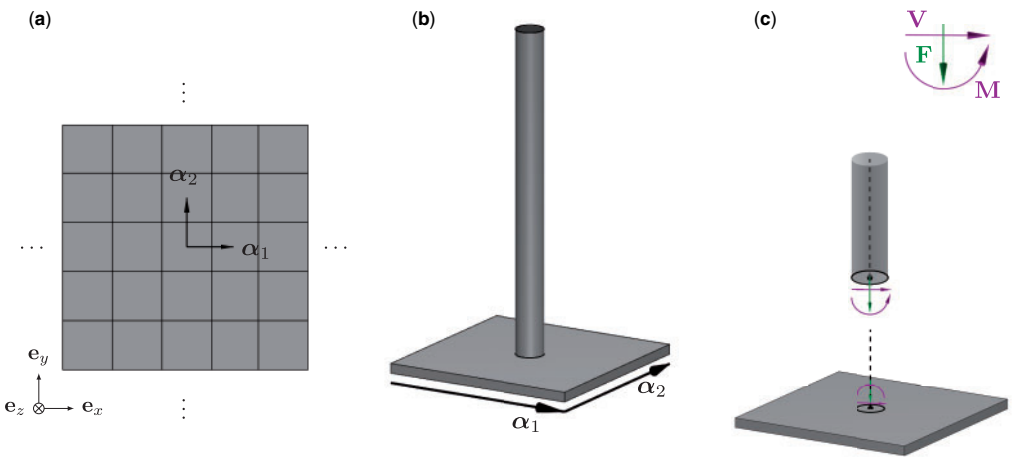

Fig. 1 A doubly periodic arrangement of beams patterning the surface of an elastic plate. Here, (a) shows the media in physical space, where the coordinate system is chosen such that the neutral plane of the elastic plate is spanned by $\mathbf{e}_x$ and $\mathbf{e}_y$ Cartesian basis vectors with $\mathbf{e}_z$ out of the page. The media is formed by a tessellation of a primitive cell, defined by the primitive lattice vectors $\boldsymbol{\alpha}_1$ and $\boldsymbol{\alpha}_2$. In (b), the simplest arrangement of one beam per primitive cell is shown. (c) The point forces and moments arising from the compressional (**F**) and shear (**V**) forces, and moments (**M**) within a beam interacting with the plate are shown.

Our Green's functions are related to those studied in (79, 80), where gyro-topped massless beams were analytically considered atop massless plates. Their Green's functions introduce similar logarithmic singularities to ours; however, their analysis was not leveraged to consider scattering simulations nor does it satisfy the Sommerfeld radiation condition in the far field. Similar to Colquitt *et al*. (78), we consider beams with mass, whose resonances manipulate waves at the subwavelength scale. In (78), only 1D arrays of beams were considered for quasi-two-dimensional (2D) media, whereas we consider 2D arrays of beams for quasi-three-dimensional (3D) media. The Green's functions of (78) were constructed from the Poisson summation formula (86) of the Fourier transformed medium; the infinite sums were analytically evaluated and the problem was shown to simplify to finding the zeros of a 3×3 determinant. The solutions to the quasi-2D problem remain well behaved even near resonance and elegantly determine the dispersive properties of the media.

Unfortunately, the quasi-3D problem is not so well behaved. To analytically model the problem, we decompose the displacement fields following Euler–Bernoulli beam theory and classical thin plate theories (87, 88), in which respective solutions vary only about the neutral axis or planes of the beams and plates. The Green's functions satisfying the time-harmonic problem contain logarithmic (79, 80, 85) and algebraic (42) singularities in the field as one approaches the centre of a beam along the neutral plane.

The singular Green's functions in Carta *et al*. (79, 80) are regularised in a manner as proposed by (82, 89) (and later in a periodic setting by (90, 91)), where one may assume sections of the plate beneath the beam are rigid and hence described by some unknown (finite) translation and rotation. The lattice sums present in (79, 80) ignore the singular behaviour of the Green's functions by regularising the solutions on the boundary of the scatterer at $r = \epsilon$. We consider the same regularisation but include in-plane motion and derive schemes in which the Green's functions behave as the singular expressions they are in the near field, and scatter energy such that the Sommerfeld radiation condition is satisfied in the far field.

We apply the approach developed by Schnitzer and Craster (85) to solve the Floquet–Bloch dispersion problem or direct scattering problems, for arrangements of scatterers which singularly perturb a wavefield. The point forcing approximations for the isotropic case in (85) was extended to consider anisotropic forcing in (42). We replace the singular asymptotic matching framework, which considered Dirichlet (85) or Neumann (42) inclusions within a Helmholtz wavefield, by assuming the displacement field at the junction (79, 80) between a beam and plate follows the hypothesis of Euler–Bernoulli beam theory (87), and hence acts like a rigid disk. We opt to simplify the analysis using the aforementioned regularisation procedure instead of considering a formal matching procedure, since a variety of asymptotic regimes exist (92).

The static problem considered in (82) is appropriate when considering the simplified junction conditions for compressional and flexural beam motion coupling into flexural plate motion.[1] Examining the singular asymptotics of our dynamic Green's function (see (2.8)), we find agreement with (82) where our dipole term w_{dipole} arising from the moment behaves like

$$w_{\text{dipole}} = \frac{\mathbf{e}_\theta \cdot \mathbf{M}(\Omega)}{8D}\left[\frac{2}{\pi}\left(\log\frac{r\sqrt{\Omega}}{2} + \gamma_E - \frac{1}{2}\right) - \frac{i}{2}\right] r + \mathcal{O}(r^3), \qquad \text{as } r \to 0, \tag{2.1}$$

[1] Refer to §63 and $w = w_0 + w_1$ in (82) for assumptions and conditions on the boundary of rigid scatterers under forcing, and §75 for derivation of the asymptotics of the Green's functions for point forces (w_0) and moments (w_1) applied to the surface of an elastic plate.

where γ_E is the Euler–Mascheroni constant. Therefore, the moment term produces a logarithmic singularity in the gradient of the flexural displacement field of the plate as $r \to 0$, the components of which are required for continuity of rotation. The related works of Mead (**93**) and Mace (**94**) also consider the quasi-3D analogue of (**78**) by employing integral transform techniques and applying the Poisson summation formula to derive the solution. The treatment of the summations within (**93**) and (**94**) simply truncate the conditionally convergent series and hence ignore the singular asymptotics of ∇w_{dipole}; as a result, their solutions are only appropriate away from flexural dominated regimes of motion within the beams.

2.1 *Doubly periodic arrangements of beams atop an elastic plate*

We model the beams using Euler–Bernoulli beam theory—see appendix section A (A.7) and (A.8) satisfying the boundary conditions (A.9) and (A.11) for details. The forces and moments arising from the beams, applied to the surface of the plate, may be analytically expressed in terms of unknown plate quantities; henceforth, we approximate each beam by point monopole and dipole source terms, whose coefficients are carefully determined to satisfy conservation of displacements, rotations, forces and moments where each beam meets the plate. For any arbitrary doubly periodic arrangement of beams, we consider N primitive cells, each of which containing P beams. We introduce $I = 1, \dots, N$ and $J = 1, \dots, P$ to enumerate quantities belonging to the IJth beam by subscript IJ, and follow (**79**, **80**, **95**) for the convention of moments arising from the beams.

The displacement field of the plate is modelled using classical thin plate theories for plate bending and extension, and is regarded as a superposition of: Kirchhoff–Love plate theory for flexural motion arising from pure bending deformations (**87**, **88**), and a 2D elastic field in plane stress arising from purely longitudinal deformations in the plane of the plate (**88**, **96**). Refer to the appendix A (A.2) for the assumed form of the displacement field, and (A.5) and (A.6) for the expressions governing the displacement field of the plate. The plate is assumed to be sufficiently thin such that the Kirchhoff–Love plate theory is valid and that the purely longitudinal deformations are uniform across the plate thickness. Hence, the longitudinal deformations result in a plane stress field which does not contribute to plate bending. We consider the problem in the time-harmonic regime. Using the point force and moment approximations of the beams, the following dimensionless system governs the displacement field of the plate

$$\left[\nabla^4 - \Omega^2\right] \mathbf{w} = \frac{1}{D} \sum_{I=1}^{N} \sum_{J=1}^{P} L\mathbf{F}_{IJ}\delta(\mathbf{x} - \mathbf{X}_{IJ}) - \mathbf{M}_{IJ} \wedge \nabla\delta(\mathbf{x} - \mathbf{X}_{IJ}), \tag{2.2}$$

$$\left[\nabla^2 + \frac{\Omega^2 h^2}{12L^2}\right] \phi = \frac{12L}{\rho\Omega^2 h^3} \frac{1}{\alpha^2} \sum_{I=1}^{N} \sum_{J=1}^{P} \nabla \cdot \mathbf{V}_{IJ}\delta(\mathbf{x} - \mathbf{X}_{IJ}), \tag{2.3}$$

$$\left[\nabla^2 + \frac{\Omega^2 h^2}{12L^2} \frac{\alpha^2}{\beta^2}\right] \boldsymbol{\psi} = -\frac{12L}{\rho\Omega^2 h^3} \frac{1}{\alpha^2} \sum_{I=1}^{N} \sum_{J=1}^{P} \nabla \wedge \mathbf{V}_{IJ}\delta(\mathbf{x} - \mathbf{X}_{IJ}). \tag{2.4}$$

Here, we respectively denote $\mathbf{w} = w\mathbf{e}_z$, ϕ and $\boldsymbol{\psi} = \psi\mathbf{e}_z$ as the dimensionless out-of-plane displacement, and the dilational and shear potentials in the x–y plane. The dilational and shear components of $\mathbf{V}_{IJ}$ coupling into ϕ and $\boldsymbol{\psi}$ have been determined by inspection of equation (A.6) as in (**97**). Additionally, in (2.2)–(2.4), we denote L as some characteristic length scale, $\Omega^2 = \omega^2 \frac{\rho h L^4}{D}$

the dimensionless frequency parameter, $\alpha^2 = \frac{4\mu(\lambda+\mu)}{\rho(\lambda+2\mu)} = \frac{E}{\rho(1-\nu^2)}$ and $\beta^2 = \frac{\mu}{\rho} = \frac{1}{2}\frac{E}{\rho(1+\nu)}$ denote the dilational (P) and shear (S) wave speeds (squared) for elastic waves propagating in the plane of a thin elastic plate in plane stress (**88**, **96**). We define dimensionless quantities $\hat{\alpha}^2 = \frac{\hat{\rho}}{\hat{E}}\frac{D}{\rho h L^2}$ and $\hat{\beta}^4 = \frac{\hat{\rho}\hat{S}}{\hat{E}\hat{I}}\frac{D}{\rho h}$ within the beams. λ and μ denote the Lamè constants of the plate of thickness h, flexural rigidity $D = \frac{Eh^3}{12(1-\nu^2)}$ and Poisson's ratio ν. Further, we denote ρ as the density, E Young's Modulus, S cross-sectional area and I the second moment of area of either the plate (regular quantities) or the beams (hatted quantities). We denote ϵ_{IJ} as the dimensionless cross-sectional radius of the beams. Throughout, $\nabla = \mathbf{e}_x\frac{\partial}{\partial x} + \mathbf{e}_y\frac{\partial}{\partial y}$ denotes the in-plane 2D gradient and $\mathbf{x} = x\mathbf{e}_x + y\mathbf{e}_y$ denotes the in-plane position. Lastly, $\delta(\mathbf{x})$ denotes the Dirac delta function.

We work in a regime where $\epsilon_{IJ} \ll \min(|\boldsymbol{\alpha}_1|, |\boldsymbol{\alpha}_2|)$ and $\epsilon_{IJ}\Omega \ll 1$. The asymptotic limit we consider is $\epsilon_{IJ} \to 0$, and we assume frequencies are not too high, and hence wavelengths not too small, such that the asymptotics in Appendix C holds and any expansions of Bessel or Hankel functions remain accurate. The thickness of the plate h is considered small such that the classical thin plate theories used are valid, however h is not of importance within our asymptotics (compare the parameters and analytical solutions of Figs 2 and 3 for instance).

The source terms $\mathbf{F}_{IJ}$, $\mathbf{M}_{IJ}$ and $\mathbf{V}_{IJ}$ are given by the forces and moments at the base of the beams. They are deduced by solving the equations governing displacement in the beams, satisfying free-end conditions at the free end and continuity of displacements and rotations at the other. Hence, by solving (A.7) and (A.8) subject to the boundary conditions (A.9) and (A.11), and by utilising these solutions within the following definitions of forces and moments within the beams (**87**, **88**) we find

$$\mathbf{F}(\Omega) = -\hat{S}\hat{E}\frac{\partial\hat{\mathbf{w}}}{\partial z}\Big|_{z=\frac{h}{2L}} = \hat{S}\hat{E}\hat{\alpha}\Omega\tan(\hat{\alpha}\Omega\hat{\ell})\mathbf{w}(\mathbf{X}), \tag{2.5}$$

$$\mathbf{M}(\Omega) = \frac{\hat{E}\hat{I}}{L}\frac{\partial}{\partial z}\Big[\nabla\wedge\hat{\mathbf{u}}\Big]\Big|_{z=\frac{h}{2L}} = \\ = \frac{\hat{E}\hat{I}}{L}\frac{\hat{\beta}\sqrt{\Omega}\Big[\nabla\wedge\mathbf{w}\Big]\Big|_{\mathbf{x}=\mathbf{X}}\left\{\begin{array}{l}\frac{h}{2L}\hat{\beta}\sqrt{\Omega}\sin\hat{\beta}\sqrt{\Omega}\hat{\ell}\tanh\hat{\beta}\sqrt{\Omega}\hat{\ell} \\ \quad +2\Big(\sin\hat{\beta}\sqrt{\Omega}\hat{\ell} - \cos\hat{\beta}\sqrt{\Omega}\hat{\ell}\tanh\hat{\beta}\sqrt{\Omega}\hat{\ell}\Big)\end{array}\right\}}{\cos\hat{\beta}\sqrt{\Omega}\hat{\ell} + \operatorname{sech}\hat{\beta}\sqrt{\Omega}\hat{\ell}}, \tag{2.6}$$

$$\mathbf{V}(\Omega) = -\frac{\hat{E}\hat{I}}{L^2}\frac{\partial^3\hat{\mathbf{u}}}{\partial z^3}\Big|_{z=\frac{h}{2L}} = \\ = -\frac{\hat{E}\hat{I}}{L^2}\frac{\hat{\beta}^2\Omega\Big[\nabla\mathbf{w}\Big]\Big|_{\mathbf{x}=\mathbf{X}}\left\{\begin{array}{l}2\sin\hat{\beta}\sqrt{\Omega}\hat{\ell}\tanh\hat{\beta}\sqrt{\Omega}\hat{\ell} \\ \quad +\frac{h}{2L}\hat{\beta}\sqrt{\Omega}\Big(\cos\hat{\beta}\sqrt{\Omega}\hat{\ell}\tanh\hat{\beta}\sqrt{\Omega}\hat{\ell} + \sin\hat{\beta}\sqrt{\Omega}\hat{\ell}\Big)\end{array}\right\}}{\cos\hat{\beta}\sqrt{\Omega}\hat{\ell} + \operatorname{sech}\hat{\beta}\sqrt{\Omega}\hat{\ell}}. \tag{2.7}$$

In the above, for brevity, we shall assume $P = 1$ knowing that generalisations to consider arbitrary P are trivial for the techniques we use; subsequently, it is sufficient to consider the contribution from the $\mathbf{x} = \mathbf{X}$th beam and drop any subscript IJ and any summations over IJ. These subscripts

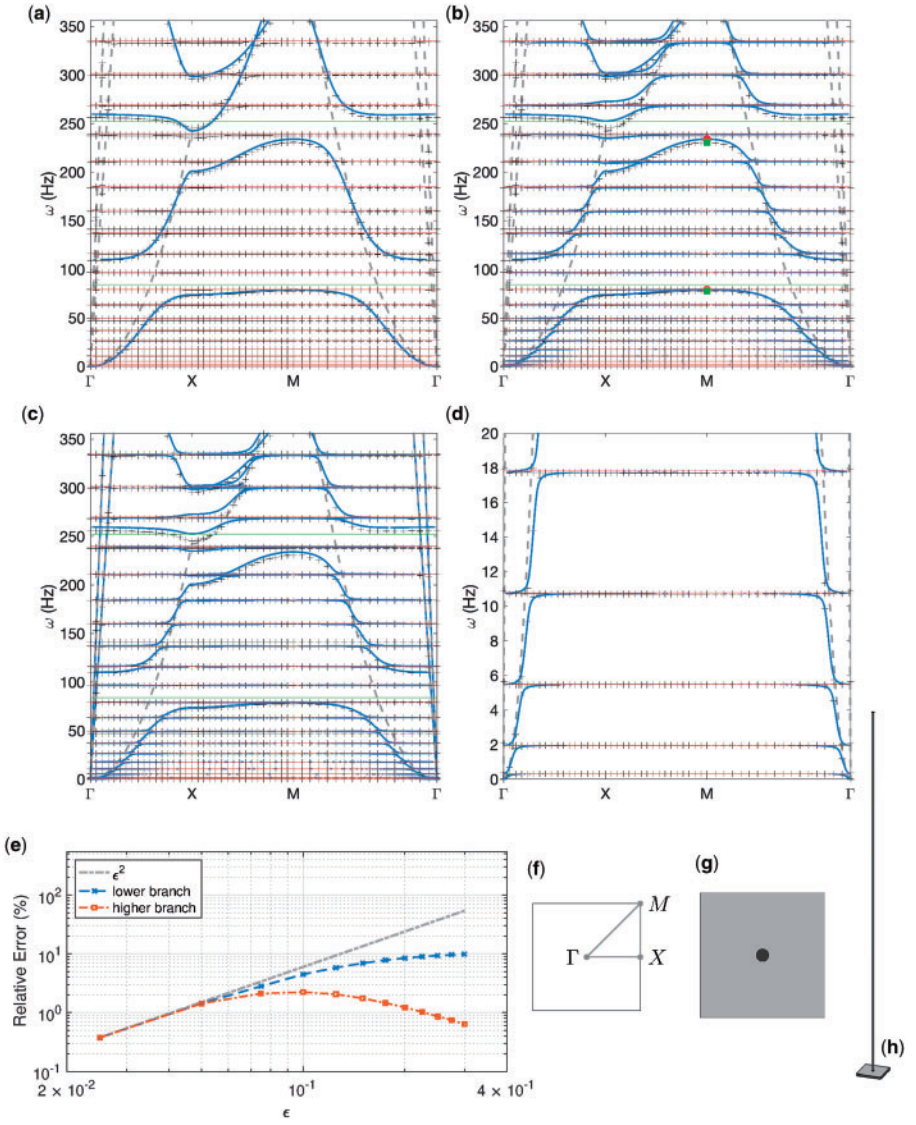

Fig. 2 Comparisons of the dispersion curves computed from the eigenvalue problem (D.2) (blue dots) and FEM computations (black crosses) for the primitive cell given in panels (g) (top view) and (h) (side view). Here, $h = 0.1$ m and the dimensionless parameters (scaled with L) are: $\boldsymbol{\alpha}_1 = \mathbf{e}_x$, $\boldsymbol{\alpha}_2 = \mathbf{e}_y$, $\epsilon = 0.05$, $\hat{\ell} = 15$. (a), (b) and (c) Consider cases 1, 2 and 3 respectively, (d) shows a zoomed in section of the flexural resonances from (b) were grey dashed lines in (a)–(d) represents the flexural (lowest), shear (middle) and dilational (highest) free space 'light' lines. Here, $\omega = \omega(\boldsymbol{\kappa})$ is plotted throughout the irreducible Brillouin zone (f). The green and red lines correspond to the resonances from (5.1) and (5.2), respectively. (e) The relative error found when comparing the frequencies highlighted in (b), comparing red circles with green squares on the lower and higher branches, and how this error evolves changing only ϵ for analogous eigenmodes.

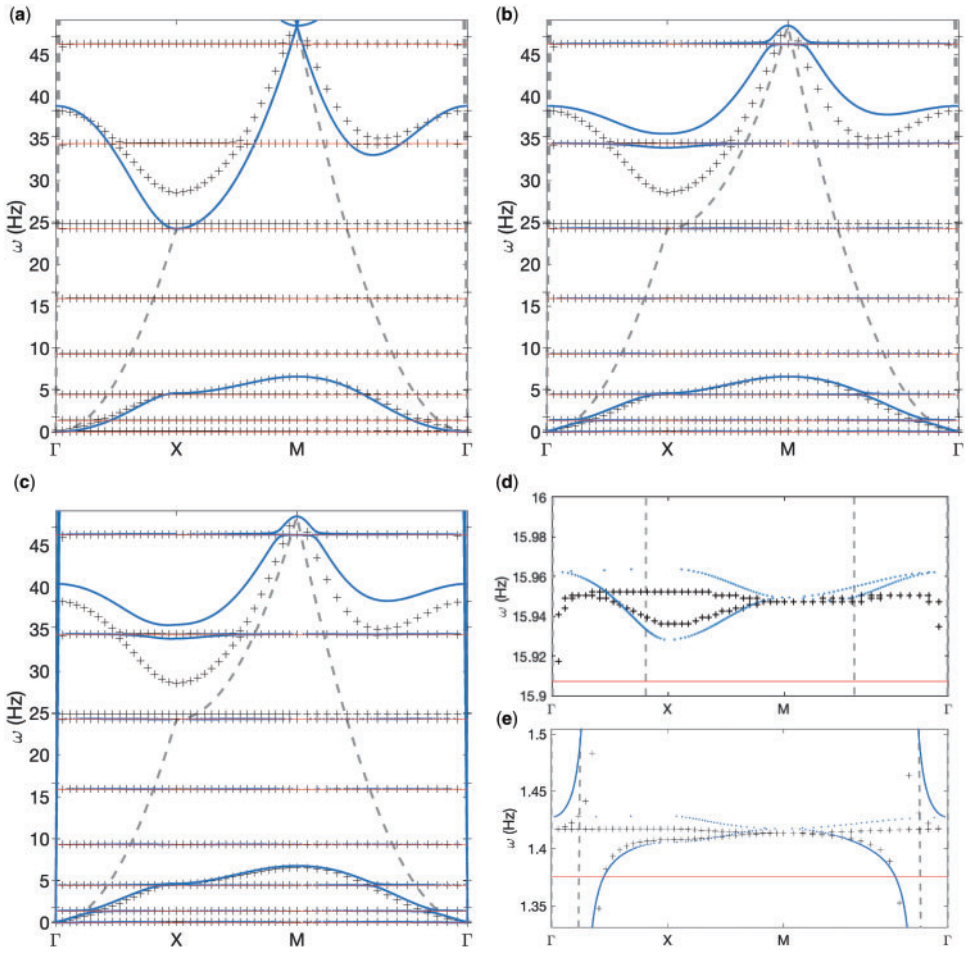

Fig. 3 Same as Fig. 2, but with $h = 0.01$ m and the red lines corresponding to resonances from (5.3). Here, (d) and (e) show zoomed in sections of the resonances from (b).

and sums will be reinstated as required to consider the contributions of more beams. In (2.6), we require $\mathbf{u}(\mathbf{X}) = \mathbf{0}$ to satisfy continuity of moments, otherwise the bending moment coupling into the plate cannot be attributed to pure plate bending. If $\mathbf{u}(\mathbf{X})$ is assumed arbitrary then the moment $\mathbf{M}$ conserved within the plate is given by (A.13), which has contributions from the purely longitudinal plate motion and hence contradicts the assumptions within the applied thin plate theory. The system (2.2)–(2.4) can be solved for N finite or infinite, depending on how one treats the unknowns. In section 3, we treat N as infinite and, through the use of Floquet–Bloch analysis, express the solution through the fundamental cell (where $I = 1$) as a polynomial eigenvalue problem. In section 4, we treat N as finite and express the solution for direct scattering simulations in the unbounded $\mathbf{x}$ space, utilising generalised Foldy's method.

The Green's functions satisfying (2.2)–(2.4) may be determined using the Fourier transform (**42**, **87**, **98**), where we find

$$w = \frac{L}{D}F(\Omega)\Big[H_0(r\sqrt{\Omega}) - H_0(ir\sqrt{\Omega})\Big]\frac{i}{8\Omega} - \frac{\mathbf{e}_\theta \cdot \mathbf{M}(\Omega)}{D}\Big[iH_1(r\sqrt{\Omega}) + H_1(ir\sqrt{\Omega})\Big]\frac{1}{8\sqrt{\Omega}}, \tag{2.8}$$

$$\phi = \frac{i\sqrt{3}}{2}\frac{\mathbf{e}_r \cdot \mathbf{V}(\Omega)}{\rho\Omega h^2\alpha^2}H_1(\frac{\Omega h}{2L\sqrt{3}}r), \tag{2.9}$$

$$\psi = \frac{\sqrt{3}}{2i}\frac{\mathbf{e}_\theta \cdot \mathbf{V}(\Omega)}{\rho\Omega h^2\alpha\beta}H_1(\frac{\alpha}{\beta}\frac{\Omega h}{2L\sqrt{3}}r). \tag{2.10}$$

Here, we denote $H_n(x) = H_n^{(1)}(x)$ to be Hankel functions of the first kind and nth order—we suppress the superscript (1) since we only consider Hankel functions of the first kind, those which correspond to scattered waves outgoing at infinity and satisfy the Sommerfeld radiation condition. Note (2.8) contains logarithmically singular terms within its gradient, as in (2.1). Since the components of ∇w are required in the forcing terms (2.6) and (2.7), we must examine ∇w in the limit as $r \to 0$. Information about the gradients of the field are often required when determining eigensolutions or direct scattering from small anisotropic scatterers (**42**, **83**). In (**42**), the method of matched asymptotic expansions (**85**, **99**, **100**) was applied to construct 'inner' and 'outer' expansions, each expansion of which has an associated region of validity and these solutions were matched where such regions overlap.

When considering a thin beam attached to a thin elastic plate, many parameters could be small (ϵ, h, Ω) or large (source terms (2.6)–(2.7) approaching resonance), meaning many different asymptotic regimes could exist and complicate a formal asymptotic matching procedure. However, the behaviour of the scatterer for $r \leq \epsilon$ can be approximated by using simplified junction conditions (**79**, **80**). Subsequently, we no longer require an inner solution, and can simply equate the Fourier series and transform representations of the Green's functions as $r \to 0$; similarly to (**42**), the singular asymptotics of both of these representations are identical and hence cancel, allowing an eigenvalue problem to be constructed to determine dispersion. This approach is also naturally applicable within Foldy's method to determine scattering from finite collections of scatterers.

When deriving (A.7) and (A.8), two main assumptions have been made about beam motion. Firstly, the analytical solution completely ignores rotary inertia and hence neglects torsion about the axis of the beam—in the low frequency regime, torsional deformations are expected to be negligible. To test this assumption, both rotary inertia and torsional beam deformations are included within the FEM model that we compare our analytical solutions to (see section 5). Secondly, shear deformations within beams are also neglected; that is, cross-sections perpendicular to the neutral axis of the undeformed problem will always remain plane and perpendicular to the neutral axis during deformation (**87**). Under these assumptions, an asymptotically formal inner solution may be replaced by considering the beam-plate intersection as rigid (**82**, **89**–**91**). We subsequently alter our matching procedure in (**42**) to regularise the problem in a similar fashion to (**79**, **80**), by introducing a rigid disk characterised by a finite, but unknown, displacement $w(\mathbf{X})$ and rotation $\Big[\nabla \wedge \mathbf{w}\Big]\Big|_{\mathbf{x}=\mathbf{X}}$

$$w = w(\mathbf{X}) - r\mathbf{e}_\theta \cdot \left(\Big[\nabla \wedge \mathbf{w}\Big]\Big|_{\mathbf{x}=\mathbf{X}}\right) \qquad \text{for } r \leq \epsilon, \tag{2.11}$$

$$\mathbf{u} = \mathbf{0} \qquad \text{for } r \leq \epsilon. \tag{2.12}$$

Condition (2.12) arises from assuming both $\mathbf{u}(\mathbf{X}) = \mathbf{0}$ and (A.12), as required for consistency from (2.5)–(2.7) and the continuity condition (A.12).

2.2 *Green's functions incorporating boundary conditions*

The Green's functions (2.8)–(2.10) satisfy the forced equations (2.2)–(2.4); their current form ignores the physical behaviour of the actual scatterer about $r = \epsilon$. Hence, we require from (2.11)

$$w\Big|_{r=\epsilon} = w(\mathbf{X}) - \epsilon \mathbf{e}_\theta \cdot \left(\Big[\!\Big[\nabla \wedge \mathbf{w} \Big]\!\Big]\Big|_{\mathbf{x}=\mathbf{X}} \right), \tag{2.13}$$

$$\frac{\partial w}{\partial r}\Big|_{r=\epsilon} = -\mathbf{e}_\theta \cdot \left(\Big[\!\Big[\nabla \wedge \mathbf{w} \Big]\!\Big]\Big|_{\mathbf{x}=\mathbf{X}} \right). \tag{2.14}$$

Furthermore, our potentials need to be consistent with (2.12), and hence we set

$$\phi\Big|_{r=\epsilon} = \Phi(\mathbf{X}), \qquad \psi\Big|_{r=\epsilon} = \Psi(\mathbf{X}). \tag{2.15}$$

Currently, (2.8)–(2.10) solve the inhomogeneous equations (2.2)–(2.4). We consider the complementary solutions to the homogeneous part of these equations where, for a certain choice of constants, the above conditions are satisfied and a solution with the correct behaviour as $r \to \infty$ constructed. We make the assumption that the complementary solution quickly decays to zero, therefore in the far field only (2.8)–(2.10) remain and hence the Sommerfeld radiation condition is satisfied. Consider

$$w = w_P + w_C, \quad \phi = \phi_P + \phi_C, \quad \psi = \psi_P + \psi_C, \tag{2.16}$$

where subscript P and C terms respectively denote the particular and complementary solutions of (2.2)–(2.4). We assume the complementary solutions are finite and will behave as follows, provided r is small

$$w_C = A_0 J_0(\sqrt{\Omega} r) + B_0 J_0(i\sqrt{\Omega} r) + \mathbf{e}_\theta \cdot \mathbf{A} J_1(\sqrt{\Omega} r) + \mathbf{e}_\theta \cdot \mathbf{B} J_1(i\sqrt{\Omega} r), \tag{2.17}$$

$$\phi_C = C J_0\left(\frac{\Omega h}{2L\sqrt{3}} r \right) + \mathbf{e}_r \cdot \mathbf{C} J_1\left(\frac{\Omega h}{2L\sqrt{3}} r \right), \tag{2.18}$$

$$\psi_C = D J_0\left(\frac{\alpha}{\beta} \frac{\Omega h}{2L\sqrt{3}} r \right) + \mathbf{e}_\theta \cdot \mathbf{D} J_1\left(\frac{\alpha}{\beta} \frac{\Omega h}{2L\sqrt{3}} r \right). \tag{2.19}$$

The coefficients of the above are chosen such that (2.13)–(2.15) are satisfied and are given in Appendix B. For $r > \epsilon$ these complementary solutions are ignored–they should be thought of as standing waves existing only in the vicinity of the scatterer, in order to apply conditions (2.13)–(2.15) and not invalidate the Sommerfeld radiation condition at infinity (**42**).

3. An eigenvalue problem for periodic infinite arrays

In this section, we assume N from equations (2.2)–(2.4) is infinite and that the centroid of each primitive cell, in Fig. 1, coincides with the vertices of the following 2D Bravais lattice

$$\mathbf{R} = n\boldsymbol{\alpha}_1 + m\boldsymbol{\alpha}_2, \tag{3.1}$$

for arbitrary integers n and m. We also define $\boldsymbol{\beta}_1$ and $\boldsymbol{\beta}_2$ as a basis in reciprocal space, satisfying the following orthogonality condition

$$\boldsymbol{\alpha}_i \cdot \boldsymbol{\beta}_j = 2\pi\delta_{ij} \quad \text{for } i,j = 1,2. \tag{3.2}$$

Here, δ_{ij} denotes the Kronecker delta function. Similarly, we can define the reciprocal lattice vector

$$\mathbf{G} = n\boldsymbol{\beta}_1 + m\boldsymbol{\beta}_2, \tag{3.3}$$

again for arbitrary integers n and m. By Bloch's theorem (**76**, **77**), waves propagating through the periodic medium satisfy the Floquet–Bloch conditions

$$w = W(\mathbf{x})\exp(i\boldsymbol{\kappa}\cdot\mathbf{x}), \quad \phi = \Phi(\mathbf{x})\exp(i\boldsymbol{\kappa}\cdot\mathbf{x}), \quad \psi = \Psi(\mathbf{x})\exp(i\boldsymbol{\kappa}\cdot\mathbf{x}), \tag{3.4}$$

$$\text{where} \quad W(\mathbf{x}) = W(\mathbf{x}+\mathbf{R}), \qquad \Phi(\mathbf{x}) = \Phi(\mathbf{x}+\mathbf{R}), \qquad \Psi(\mathbf{x}) = \Psi(\mathbf{x}+\mathbf{R}). \tag{3.5}$$

Here, $\boldsymbol{\kappa}$ is the Bloch-wavevector and W, Φ and Ψ are periodic functions whose fundamental period coincides with that of the lattice (3.1). The solutions of W, Φ and Ψ are, therefore, naturally expressed by a Fourier series

$$W(\mathbf{x}) = \sum_{\mathbf{G}} W_{\mathbf{G}}\exp(i\mathbf{G}\cdot\mathbf{x}), \quad \Phi(\mathbf{x}) = \sum_{\mathbf{G}} \Phi_{\mathbf{G}}\exp(i\mathbf{G}\cdot\mathbf{x}), \quad \Psi(\mathbf{x}) = \sum_{\mathbf{G}} \Psi_{\mathbf{G}}\exp(i\mathbf{G}\cdot\mathbf{x}), \tag{3.6}$$

where $W_{\mathbf{G}}$, $\Phi_{\mathbf{G}}$ and $\Psi_{\mathbf{G}}$ denote Fourier coefficients of the expanded variables. We seek solutions to w, ϕ and ψ in the form of (3.4). The forces and moments in (2.5)–(2.7) can also be expressed using equation (3.4), as follows

$$\mathbf{F}(\Omega,\boldsymbol{\kappa}) = \mathbf{F}_p(\Omega)\exp(i\boldsymbol{\kappa}\cdot\mathbf{X}), \quad \mathbf{M}(\Omega,\boldsymbol{\kappa}) = \mathbf{M}_p(\Omega,\boldsymbol{\kappa})\exp(i\boldsymbol{\kappa}\cdot\mathbf{X}), \quad \mathbf{V}(\Omega,\boldsymbol{\kappa}) = \mathbf{V}_p(\Omega,\boldsymbol{\kappa})\exp(i\boldsymbol{\kappa}\cdot\mathbf{X}). \tag{3.7}$$

Also, A_0, B_0, $\mathbf{A}$, $\mathbf{B}$, $\mathbf{C}$ and $\mathbf{D}$ (see Appendix B) can be expressed in terms of equation (3.4) as

$$A_0 = A_{0p}\exp(i\boldsymbol{\kappa}\cdot\mathbf{X}), \tag{3.8}$$

similarly for the other coefficients in (2.17)–(2.19). Utilising (3.7) and (3.6) within (2.2)–(2.4), multiplying by $\exp(-i\mathbf{K}_{\mathbf{G}'}\cdot\mathbf{x})$ and integrating over the fundamental cell one finds, by orthogonality

$$\Big[(\mathbf{K}_{\mathbf{G}}\cdot\mathbf{K}_{\mathbf{G}})^2 - \Omega^2\Big]\mathbf{W}_{\mathbf{G}} = \frac{1}{\mathscr{A}D}\Big[L\mathbf{F}_p - i\mathbf{M}_p\wedge\mathbf{K}_{\mathbf{G}}\Big]\exp(-i\mathbf{G}\cdot\mathbf{X}), \tag{3.9}$$

$$i\mathscr{A}\alpha^2\frac{\rho\Omega^2h^3}{12L}\Big[\mathbf{K}_{\mathbf{G}}\cdot\mathbf{K}_{\mathbf{G}} - \frac{\Omega^2h^2}{12L^2}\Big]\Phi_{\mathbf{G}} = \mathbf{K}_{\mathbf{G}}\cdot\mathbf{V}_p\exp(-i\mathbf{G}\cdot\mathbf{X}), \tag{3.10}$$

$$i\mathscr{A}\alpha^2\frac{\rho\Omega^2h^3}{12L}\Big[\mathbf{K}_{\mathbf{G}}\cdot\mathbf{K}_{\mathbf{G}} - \frac{\Omega^2h^2}{12L^2}\frac{\alpha^2}{\beta^2}\Big]\boldsymbol{\Psi}_{\mathbf{G}} = -\mathbf{K}_{\mathbf{G}}\wedge\mathbf{V}_p\exp(-i\mathbf{G}\cdot\mathbf{X}). \tag{3.11}$$

Here, $\mathscr{A}$ is the physical area of the fundamental cell and $\mathbf{K}_{\mathbf{G}} = \boldsymbol{\kappa} + \mathbf{G}$. Notably, the $\exp(i\boldsymbol{\kappa}\cdot\mathbf{X})$ terms cancel from these equations governing the Fourier coefficients. Say we wish to include M modes within (3.6), we have expressed our linear system of differential equations as a system of equations

and unknowns. The unknowns in our system (3.9)–(3.11) from w are $W(\mathbf{X})$, $\partial_x W(\mathbf{X})$, $\partial_y W(\mathbf{X})$ and $W_{\mathbf{G}_i}$ for $i = 1, \ldots M$; similar unknowns exist for ϕ and ψ (without gradient terms), and we currently have a total of $3M$ equations for $3M + 5P$ unknowns. The other $5P$ equations come from inserting (3.9)–(3.11) into the Fourier expanded versions of (3.4) and examining w, ∇w, ϕ and ψ all in the limit as $\mathbf{x} \to \mathbf{X}$, or equivalently $r \to 0$, for each beam in the fundamental cell.

3.1 *The limit of Green's functions as $r \to 0$*

The Green's functions (2.8)–(2.10) and (3.4) are two different representations of our solution. The singular asymptotics of expressions (2.9)–(2.10) and ∇(2.8) have at best $\log(r)$, and at worst $\frac{1}{r}$ behaviour as $r \to 0$. Similarly, the series representations (inserting (3.6) in (3.4)) are conditionally convergent, where at $\mathbf{x} = \mathbf{X}$ the exponential terms stop oscillating and the series diverge. However, as $r \to 0$, both the Fourier series and Hankel function representations of our solutions will diverge to the same value, and singularities in r can be carefully arranged such that they cancel.

We introduce some $R \gg 1$ denoting a truncation radius in Fourier space containing M modes, and split the Fourier series expansions as follows:

$$w = w_{\text{tr}} + w_{\text{res}}, \qquad \phi = \phi_{\text{tr}} + \phi_{\text{res}}, \qquad \psi = \psi_{\text{tr}} + \psi_{\text{res}}, \tag{3.12}$$

$$\text{here} \quad w_{\text{tr}} = \sum_{|\mathbf{G}|<R} W_{\mathbf{G}} \exp(i\mathbf{K}_{\mathbf{G}} \cdot \mathbf{x}), \quad w_{\text{res}} = \sum_{|\mathbf{G}|>R} W_{\mathbf{G}} \exp(i\mathbf{K}_{\mathbf{G}} \cdot \mathbf{x}). \tag{3.13}$$

The series for ϕ and ψ are split up in an identical fashion to expression (3.13), where subscript tr and res terms respectively denote the truncated and residual portion of the series before and after the truncation position R. Examining $\lim_{r\to 0} \exp(-i\boldsymbol{\kappa} \cdot \mathbf{x})\cdot$(3.12) we find

$$\lim_{r\to 0} \sum_{|\mathbf{G}|<R} W_{\mathbf{G}} \exp(i\mathbf{G} \cdot \mathbf{x}) = W(\mathbf{X}), \tag{3.14}$$

indeed since the $\lim_{r\to 0} w_{\text{res}} = 0$. Additionally, we consider the following, all in the limit as $r \to 0$

$$\exp(-i\boldsymbol{\kappa} \cdot \mathbf{x})\nabla\Big[w - w_{\text{res}}\Big] = \exp(-i\boldsymbol{\kappa} \cdot \mathbf{x})\nabla w_{\text{tr}}, \tag{3.15}$$

$$\exp(-i\boldsymbol{\kappa} \cdot \mathbf{x})\Big[\phi - \phi_{\text{res}}\Big] = \exp(-i\boldsymbol{\kappa} \cdot \mathbf{x})\phi_{\text{tr}}, \tag{3.16}$$

$$\exp(-i\boldsymbol{\kappa} \cdot \mathbf{x})\Big[\psi - \psi_{\text{res}}\Big] = \exp(-i\boldsymbol{\kappa} \cdot \mathbf{x})\psi_{\text{tr}}. \tag{3.17}$$

By substituting the required expressions from (3.12), (2.16) and appendix section C into the above, expanding the Bessel (and integral Bessel (C.1)) functions and Hankel functions as $r \to 0$, and assuming $rR \ll 1$, the following expressions can be found

$$\lim_{r\to 0} \mathbf{e}_x \cdot \sum_{|\mathbf{G}|<R} i\mathbf{K}_{\mathbf{G}} W_{\mathbf{G}} \exp(i\mathbf{G} \cdot \mathbf{x}) = -\frac{\mathbf{e}_y \cdot \mathbf{M}_p}{4\pi D}\Big[\log\frac{\epsilon R}{2} + \gamma_E - 1\Big] + W_x(\mathbf{X}) + i\kappa_1 W(\mathbf{X}), \tag{3.18}$$

$$\lim_{r\to 0} \mathbf{e}_y \cdot \sum_{|\mathbf{G}|<R} i\mathbf{K}_{\mathbf{G}} W_{\mathbf{G}} \exp(i\mathbf{G} \cdot \mathbf{x}) = \frac{\mathbf{e}_x \cdot \mathbf{M}_p}{4\pi D}\Big[\log\frac{\epsilon R}{2} + \gamma_E - 1\Big] + W_y(\mathbf{X}) + i\kappa_2 W(\mathbf{X}), \tag{3.19}$$

$$\lim_{r\to 0}\frac{\rho\Omega^2h^3}{12L}\sum_{|\mathbf{G}|<R}\Phi_{\mathbf{G}}\exp(i\mathbf{G}\cdot\mathbf{x})=\frac{1}{\alpha^2}\left[\frac{\mathbf{V}_p\cdot\boldsymbol{\kappa}}{4i\pi}\right]+\frac{\rho\Omega^2h^3}{12L}\Phi(\mathbf{X}), \tag{3.20}$$

$$\lim_{r\to 0}\frac{\rho\Omega^2h^3}{12L}\sum_{|\mathbf{G}|<R}\Psi_{\mathbf{G}}\exp(i\mathbf{G}\cdot\mathbf{x})=\frac{1}{\alpha^2}\left[\frac{i(\boldsymbol{\kappa}\wedge\mathbf{V}_p)\cdot\mathbf{e}_z}{4\pi}\right]+\frac{\rho\Omega^2h^3}{12L}\Psi(\mathbf{X}). \tag{3.21}$$

Both components of $\boldsymbol{\kappa}=\boldsymbol{\kappa}(\Omega)$ are required, hence we introduce the following change of variables

$$\boldsymbol{\kappa}=\eta\Big[\cos\theta_\eta\mathbf{e}_x+\sin\theta_\eta\mathbf{e}_y\Big]+\boldsymbol{\zeta}. \tag{3.22}$$

Here, $\boldsymbol{\zeta}$ can be set to shift the origin of the wavevector to any convenient (high-symmetry) point within the Brillouin zone, θ_η set to consider any direction along said point, and η subsequently determined as the eigenvalue of such a problem for any frequency considered. Rewriting equations (3.9)–(3.11), (3.14), (3.18)–(3.21) in terms of η, one finds the following polynomial eigenvalue problem whose solution yields all unknowns in the system

$$\Big[\eta^4\mathcal{A}(\Omega)+\eta^3\mathcal{B}(\Omega)+\eta^2\mathcal{C}(\Omega)+\eta\mathcal{D}(\Omega)+\mathcal{E}(\Omega)\Big]\boldsymbol{\Theta}=\mathbf{0}. \tag{3.23}$$

Here, $\mathcal{A}$, $\mathcal{B}$, …, $\mathcal{E}$ denote matrices of dimension $(3M+5P)\times(3M+5P)$ containing various trigonometric and hyperbolic functions of Ω. The eigenvalue η is inserted into (3.22) and hence one finds $\boldsymbol{\kappa}=\boldsymbol{\kappa}(\Omega)$ by looping through all required frequencies. The eigenvector $\boldsymbol{\Theta}$ contains the $(3M+5P)$ unknowns $W_{\mathbf{G}}$'s, $\Phi_{\mathbf{G}}$'s, $\Psi_{\mathbf{G}}$'s, $W(\mathbf{X})$'s, $W_x(\mathbf{X})$'s, $W_y(\mathbf{X})$'s, $\Phi(\mathbf{X})$'s, $\Psi(\mathbf{X})$'s.

For the asymptotic analysis within Appendix C to remain accurate, one needs to ensure R and hence M is sufficiently large. Appropriate magnitudes of M depend on the problem one wishes to consider. Practically speaking, M being in the tens or hundreds gives sufficiently small errors when considering Floquet–Bloch dispersion through the fundamental cell; however, for ribbon or interfacial problems containing many cells (as in Figs 8 (*e*) or 12 (*e*)), $\mathcal{O}(M)=10^3$ is required. In such cases, the polynomial eigenvalue problem of dimension $(3M+5P)\times(3M+5P)$ will be computationally expensive to solve. However, utilising (**101**), the polynomial eigenvalue problem (3.23) can be expressed as an algebraic eigenvalue problem whose eigenvalues and eigenvectors can be computed quickly and cheaply, as shown in the Appendix section D.

4. The generalised Foldy problem: a finite arrangement of scatterers under incident forcing

Consider a phononic crystal formed from a finite portion of the infinitely repeating periodic media examined in section 3. Provided this finite section is large enough, the Floquet–Bloch waves, whose dispersion relation is a priori known by the analysis of section 3, still persist throughout the medium and hence we know how energy propagates within the crystal. Propagation about the edge of such media can also be determined (**33**) by considering conserved quantities of $\boldsymbol{\kappa}$.

In this section, we assume N from equations (2.2)–(2.4) is finite. We now consider the crystal under incidence, and derive the solutions describing the displacement fields over the entire space. In this section, we re-write the summations present in (2.2)–(2.4) as follows

$$\Big[\nabla^4-\Omega^2\Big]\mathbf{w}=\tilde{\mathbf{w}}_{\text{inc}}(\mathbf{x})+\frac{1}{D}\sum_{j=1}^{m}L\mathbf{F}_j\delta(\mathbf{x}-\mathbf{X}_j)-\mathbf{M}_j\wedge\nabla\delta(\mathbf{x}-\mathbf{X}_j), \tag{4.1}$$

$$\left[\nabla^2 + \frac{\Omega^2 h^2}{12L^2}\right]\phi = \tilde{\phi}_{\text{inc}}(\mathbf{x}) + \frac{12L}{\rho\Omega^2 h^3}\frac{1}{\alpha^2}\sum_{j=1}^{m}\nabla\cdot\mathbf{V}_j\delta(\mathbf{x}-\mathbf{X}_j), \tag{4.2}$$

$$\left[\nabla^2 + \frac{\Omega^2 h^2}{12L^2}\frac{\alpha^2}{\beta^2}\right]\boldsymbol{\psi} = \tilde{\boldsymbol{\psi}}_{\text{inc}}(\mathbf{x}) - \frac{12L}{\rho\Omega^2 h^3}\frac{1}{\alpha^2}\sum_{j=1}^{m}\nabla\wedge\mathbf{V}_j\delta(\mathbf{x}-\mathbf{X}_j), \tag{4.3}$$

Here, index j enumerates the $m = NP$ total number of beams forming the phononic crystal. Additionally, $\tilde{\mathbf{w}}_{\text{inc}}$, $\tilde{\phi}_{\text{inc}}$ and $\tilde{\boldsymbol{\psi}}_{\text{inc}}$ denotes some forcing incident upon the overall structure, the Green's functions of which we respectively denote $\mathbf{w}_{\text{inc}}$, ϕ_{inc} and $\boldsymbol{\psi}_{\text{inc}}$. Herein, we consider a purely out-of-plane monopole point source of strength ϖ_{inc}, centred on $\mathbf{x} = \mathbf{X}_{\text{inc}}$, by setting

$$\tilde{\mathbf{w}}_{\text{inc}} = \varpi_{\text{inc}}\delta(\mathbf{x}-\mathbf{X}_{\text{inc}})\mathbf{e}_z, \quad \text{and} \quad \tilde{\phi}_{\text{inc}}(\mathbf{x}) = \tilde{\psi}_{\text{inc}}(\mathbf{x}) = 0. \tag{4.4}$$

The Green's functions for the above source are given by

$$w_{\text{inc}}(\mathbf{x}) = \frac{i}{8\Omega}\varpi_{\text{inc}}\Big[H_0(|\mathbf{x}-\mathbf{X}_{\text{inc}}|\sqrt{\Omega}) - H_0(i|\mathbf{x}-\mathbf{X}_{\text{inc}}|\sqrt{\Omega})\Big], \qquad \phi_{\text{inc}} = \psi_{\text{inc}} = 0. \tag{4.5}$$

We proceed by re-writing the forcing terms from (2.5) to (2.7), as follows

$$\mathbf{F}_j(\Omega) = F_j\Omega w(\mathbf{X}_j)\mathbf{e}_z, \qquad \mathbf{M}_j = M_j\sqrt{\Omega}(\nabla\wedge\mathbf{w})\Big|_{\mathbf{x}=\mathbf{X}_j}, \qquad \mathbf{V}_j = V_j\Omega\nabla w\Big|_{\mathbf{x}=\mathbf{X}_j}, \tag{4.6}$$

where

$$F_j = \hat{S}_j\hat{E}_j\hat{\alpha}_j\tan(\hat{\alpha}_j\Omega\hat{\ell}_j), \tag{4.7}$$

$$M_j = \frac{\hat{E}_j\hat{I}_j}{L}\frac{\hat{\beta}_j\Big\{\frac{h}{2L}\hat{\beta}_j\sqrt{\Omega}\sin\hat{\beta}_j\sqrt{\Omega}\hat{\ell}_j\tanh\hat{\beta}_j\sqrt{\Omega}\hat{\ell}_j + 2\Big(\sin\hat{\beta}_j\sqrt{\Omega}\hat{\ell}_j - \cos\hat{\beta}_j\sqrt{\Omega}\hat{\ell}_j\tanh\hat{\beta}_j\sqrt{\Omega}\hat{\ell}_j\Big)\Big\}}{\cos\hat{\beta}_j\sqrt{\Omega}\hat{\ell}_j + \operatorname{sech}\hat{\beta}_j\sqrt{\Omega}\hat{\ell}_j}, \tag{4.8}$$

$$V_j = -\frac{\hat{E}_j\hat{I}_j}{L^2}\frac{\hat{\beta}_j^2\Big\{2\sin\hat{\beta}_j\sqrt{\Omega}\hat{\ell}_j\tanh\hat{\beta}_j\sqrt{\Omega}\hat{\ell}_j + \frac{h}{2L}\hat{\beta}_j\sqrt{\Omega}\Big(\cos\hat{\beta}_j\sqrt{\Omega}\hat{\ell}_j\tanh\hat{\beta}_j\sqrt{\Omega}\hat{\ell}_j + \sin\hat{\beta}_j\sqrt{\Omega}\hat{\ell}_j\Big)\Big\}}{\cos\hat{\beta}_j\sqrt{\Omega}\hat{\ell}_j + \operatorname{sech}\hat{\beta}_j\sqrt{\Omega}\hat{\ell}_j}. \tag{4.9}$$

The Green's functions governing the total displacement fields throughout the structure are as follows

$$\begin{aligned} w(\mathbf{x}) = {} & w_{\text{inc}}(\mathbf{x}) \\ & + \sum_{j=1}^{m}\left\{\frac{iL}{8D}F_j w(\mathbf{X}_j)\Big[H_0(r_j\sqrt{\Omega}) - H_0(ir_j\sqrt{\Omega})\Big]\right. \\ & \left. -\mathbf{e}_{\theta j}\cdot(\nabla\wedge\mathbf{w})\Big|_{\mathbf{x}=\mathbf{X}_j}\frac{M_j}{8D}\Big[iH_1(r_j\sqrt{\Omega}) + H_1(ir_j\sqrt{\Omega})\Big]\right\}, \end{aligned} \tag{4.10}$$

$$\phi(\mathbf{x}) = \phi_{\text{inc}}(\mathbf{x}) + \sum_{j=1}^{m} \frac{iV_j\sqrt{3}}{2\rho h^2\alpha^2}\mathbf{e}_{rj}\cdot\nabla w\Big|_{\mathbf{x}=\mathbf{X}_j} H_1\left(\frac{\Omega h}{2L\sqrt{3}}r_j\right), \tag{4.11}$$

$$\psi(\mathbf{x}) = \psi_{\text{inc}}(\mathbf{x}) - \sum_{j=1}^{m} \frac{iV_j\sqrt{3}}{2\rho h^2\alpha\beta}\mathbf{e}_{\theta j}\cdot\nabla w\Big|_{\mathbf{x}=\mathbf{X}_j} H_1\left(\frac{\alpha}{\beta}\frac{\Omega h}{2L\sqrt{3}}r_j\right). \tag{4.12}$$

Here, $\mathbf{e}_{rj}$ and $\mathbf{e}_{\theta j}$ are the local radial polar coordinate basis vectors centred on $\mathbf{x} = \mathbf{X}_j$ and $r_j = |\mathbf{x} - \mathbf{X}_j|$. We apply Foldy's method (**102**) in which singularities, as $r_j \to 0$, are naturally removed by examining the external field. Foldy's hypothesis (**102**) states that the 'strength' of the scattered field is proportional to the external field; the constant of proportionality, known as the scattering coefficient, is typically leveraged to determine all unknowns in the system—as in (**42**, **84**). The approach taken by Schnitzer and Craster (**85**) is much more straightforward and requires examination of the external field via matched asymptotic analysis, revealing a system of linear equations readily solved by inverting a matrix.

Similarly to (**85**), we opt not to consider scattering coefficients but the external field, as defined in Appendix E (E.5)–(E.7), in the limit as $\mathbf{x}_n \to 0$. On one hand, inserting (4.10)–(4.12) into (E.5)–(E.7) we find the contribution of the nth scatter removed and the summations, as $\mathbf{x}_n \to 0$, are now finite everywhere. On the other hand, we note the singular asymptotics of the field as $r_n \to 0$ will be dominated by the nth scatterer, whose presence causes the singularities to occur—in this limit, we make use of equation (2.16) where, as $r_n \to 0$, the various finite Bessel function terms are retained in order to satisfy the conditions (2.13)–(2.15). Equating these two ways of examining the external fields, as $r_n \to 0$, one finds from (E.5), (E.6), (E.7), $\mathbf{e}_x \cdot \nabla$ (E.5) and $\mathbf{e}_y \cdot \nabla$ (E.5):

$$\left[1 - \frac{iL}{8D}F_n\right] w(\mathbf{X}_n) - \sum_{\substack{j=1\\ j\neq n}}^{m} \frac{iL}{8D}F_j w(\mathbf{X}_j)\Big[H_0(r_{nj}\sqrt{\Omega}) - H_0(ir_{nj}\sqrt{\Omega})\Big]$$

$$- \sum_{\substack{j=1\\ j\neq n}}^{m} \frac{M_j}{8D}\Big\{\cos\theta_{nj} w_x(\mathbf{X}_j) + \sin\theta_{nj} w_y(\mathbf{X}_j)\Big\}\Big[iH_1(r_{nj}\sqrt{\Omega}) + H_1(ir_{nj}\sqrt{\Omega})\Big] = w_{\text{inc}}(\mathbf{X}_n), \tag{4.13}$$

$$\phi(\mathbf{X}_n) - \sum_{\substack{j=1\\ j\neq n}}^{m} \frac{iV_j\sqrt{3}}{2\rho h^2\alpha^2}\Big\{\cos\theta_{nj} w_x(\mathbf{X}_j) + \sin\theta_{nj} w_y(\mathbf{X}_j)\Big\} H_1\left(\frac{\Omega h}{2L\sqrt{3}}r_{nj}\right) = \phi_{\text{inc}}(\mathbf{X}_n), \tag{4.14}$$

$$\psi(\mathbf{X}_n) - \sum_{\substack{j=1\\ j\neq n}}^{m} \frac{V_j\sqrt{3}}{2i\rho h^2\alpha\beta}\Big\{\cos\theta_{nj} w_y(\mathbf{X}_j) - \sin\theta_{nj} w_x(\mathbf{X}_j)\Big\} H_1\left(\frac{\alpha}{\beta}\frac{\Omega h}{2L\sqrt{3}}r_{nj}\right) = \psi_{\text{inc}}(\mathbf{X}_n). \tag{4.15}$$

$$
\begin{aligned}
&w_x(\mathbf{X}_n) + \frac{M_n\sqrt{\Omega}}{8D}\left[\frac{2}{\pi}\left(\log\frac{\epsilon_n\sqrt{\Omega}}{2} + \gamma_E - 1\right) - \frac{i}{2}\right] w_x(\mathbf{X}_n) \\
&\quad - \sum_{\substack{j=1\\ j\neq n}}^{m} \cos\theta_{nj}\frac{iL}{8D}F_j w(\mathbf{X}_j) i\sqrt{\Omega}\Big[H_1(ir_{nj}\sqrt{\Omega}) + iH_1(r_{nj}\sqrt{\Omega})\Big] \\
&\quad - \sum_{\substack{j=1\\ j\neq n}}^{m} \frac{i\cos\theta_{nj}M_j\sqrt{\Omega}}{8D}\left\{\begin{matrix}\cos\theta_{nj}w_x(\mathbf{X}_j)\\ +\sin\theta_{nj}w_y(\mathbf{X}_j)\end{matrix}\right\}\frac{\left[\begin{matrix}H_0(ir_{nj}\sqrt{\Omega}) + H_0(r_{nj}\sqrt{\Omega})\\ -H_2(ir_{nj}\sqrt{\Omega}) - H_2(r_{nj}\sqrt{\Omega})\end{matrix}\right]}{2} \\
&+ \sum_{\substack{j=1\\ j\neq n}}^{m} \frac{\sin\theta_{nj}}{r_{nj}}M_j\Big\{\cos\theta_{nj}w_y(\mathbf{X}_j) - \sin\theta_{nj}w_x(\mathbf{X}_j)\Big\}\frac{1}{8D}\Big[H_1(ir_{nj}\sqrt{\Omega}) + iH_1(r_{nj}\sqrt{\Omega})\Big] = \\
&\qquad = (\mathbf{e}_x\cdot\nabla w_{\mathrm{inc}})|_{\mathbf{x}=\mathbf{X}_n},
\end{aligned}
\tag{4.16}
$$

$$
\begin{aligned}
&w_y(\mathbf{X}_n) + \frac{M_n\sqrt{\Omega}}{8D}\left[\frac{2}{\pi}\left(\log\frac{\epsilon_n\sqrt{\Omega}}{2} + \gamma_E - 1\right) - \frac{i}{2}\right] w_y(\mathbf{X}_n) \\
&\quad - \sum_{\substack{j=1\\ j\neq n}}^{m} \sin\theta_{nj}\frac{iL}{8D}F_j w(\mathbf{X}_j) i\sqrt{\Omega}\Big[H_1(ir_{nj}\sqrt{\Omega}) + iH_1(r_{nj}\sqrt{\Omega})\Big] \\
&\quad - \sum_{\substack{j=1\\ j\neq n}}^{m} \frac{i\sin\theta_{nj}M_j\sqrt{\Omega}}{8D}\left\{\begin{matrix}\cos\theta_{nj}w_x(\mathbf{X}_j)\\ +\sin\theta_{nj}w_y(\mathbf{X}_j)\end{matrix}\right\}\frac{\left[\begin{matrix}H_0(ir_{nj}\sqrt{\Omega}) + H_0(r_{nj}\sqrt{\Omega})\\ -H_2(ir_{nj}\sqrt{\Omega}) - H_2(r_{nj}\sqrt{\Omega})\end{matrix}\right]}{2} \\
&- \sum_{\substack{j=1\\ j\neq n}}^{m} \frac{\cos\theta_{nj}}{r_{nj}}M_j\Big\{\cos\theta_{nj}w_y(\mathbf{X}_j) - \sin\theta_{nj}w_x(\mathbf{X}_j)\Big\}\frac{1}{8D}\Big[H_1(ir_{nj}\sqrt{\Omega}) + iH_1(r_{nj}\sqrt{\Omega})\Big] = \\
&\qquad = (\mathbf{e}_y\cdot\nabla w_{\mathrm{inc}})|_{\mathbf{x}=\mathbf{X}_n},
\end{aligned}
\tag{4.17}
$$

Here, θ_{nj} denotes the angle between the nth and jth scatterer, centred on $\mathbf{X}_j$ and $r_{nj} = |\mathbf{X}_n - \mathbf{X}_j|$. To find the above, Bessel functions of the first kind were asymptotically expanded as $r_{nn} \to 0$. Similarly, complementary coefficients (B.1)–(B.2) are expanded assuming ϵ_n is a small parameter. Successively considering n to take the values from 1 to m, (4.13)–(4.17) represent a system of $5m$ equations for $5m$ unknowns and are factorised as follows

$$
\mathcal{G}\boldsymbol{\Lambda} = \boldsymbol{\Lambda}_{\mathrm{inc}}. \tag{4.18}
$$

Table 1 The material parameters (**51**, **104**) used within Figs 2–13 modelling aluminium. We set $\hat{\rho}$, $\hat{E}$ and $\hat{\nu}$ to equal their unhatted counterparts within the proceeding computations. Any other required parameters will be given in the appropriate captions.

Parameter	Value
L	1 m
ρ	2710 kg m^{-3}
E	69×10^9 Pa
ν	0.33

Here, $\mathcal{G}$ represents the $5m \times 5m$ matrix formed from (4.13)–(4.17), $\mathbf{\Lambda}$ a vector containing our unknowns $w(\mathbf{X}_n)$, $\partial_x w(\mathbf{X}_n)$, $\partial_y w(\mathbf{X}_n)$, $\phi(\mathbf{X}_n)$ and $\psi(\mathbf{X}_n)$ and finally $\mathbf{\Lambda}_{\text{inc}}$ a vector containing our known incident source $w_{\text{inc}}(\mathbf{X}_n)$, $\partial_x w_{\text{inc}}(\mathbf{X}_n)$, $\partial_y w_{\text{inc}}(\mathbf{X}_n)$, $\phi_{\text{inc}}(\mathbf{X}_n)$ and $\psi_{\text{inc}}(\mathbf{X}_n)$. Once $\mathbf{\Lambda}$ is determined, the total displacement field is calculated everywhere in the phononic crystal by use of (4.10)–(4.12). The inversion of $\mathcal{G}$ is simple and accurate unless near resonance, where matrices have poor condition numbers. As in Appendix D, we opt to use the minimum norm least-squares solution to compute $\mathbf{\Lambda}$ near resonance.

5. FEM verification of the analytical solutions

In this section, we demonstrate the reliability of our analytical solutions by comparing our eigenvalues from (D.2) to FEM simulations using ABAQUS® software. The FEM simulations consider beams of finite radius, as in Fig. 1(b), to test: the accuracy of the assumed point force and moment approximation of the beams in (2.2)–(2.4), and the simplified junction conditions for $r = \epsilon$ on the plate (2.11)–(2.12). The FEM simulations model: the plate using 4-node doubly curved general-purpose shell elements and the beam using 2-node cubic beam elements. At the beam-plate interface, kinematic continuity conditions are applied which consider all components of displacement and rotation within the FEM models. Notably, the FEM analysis includes rotary inertia and torsional deformations within the beams.

Provided the dispersion relation computed from the eigenvalue problem (D.2) is accurate, our generalised Foldy solution (4.18) must also be accurate, as these two solutions are nothing more than the same Green's function written in a slightly different fashion. Additionally, one can observe whether the direct scattering solution has the same dispersive properties as predicted by the eigenvalue problem, further demonstrating the relationship of the two solutions.

Moreover, we test the model by removing various terms from the system (2.2)–(2.4), and hence various rows and columns from the matrices forming (4.18) or (D.2), to consider the following cases:

- Case 1—purely compressional forcing from the beam coupling into purely flexural motion from the plate, only (2.2) with the moment term $\mathbf{M}_{IJ}$ removed governs this case.
- Case 2—compressional and flexural forcing from the beam coupling into purely flexural motion from the plate, hence only (2.2) is included.
- Case 3—the full system (2.2)–(2.4).

Here, cases 1, 2 and 3 contain compressional resonances, arising through $\mathbf{F}$ and given by

$$\hat{\alpha}\Omega\hat{\ell} = \left(q - \frac{1}{2}\right)\pi \quad \text{for } q \in \mathbb{Z}. \tag{5.1}$$

Cases 2 and 3 also contain flexural resonances arising from $\mathbf{M}$ and $\mathbf{V}$. Figures 2 and 3 reveal two different regimes exist for the flexural resonances within the system, depending on the ratio of ϵ to h. As in Colquitt *et al*. (**78**), when the plate is thicker than the beam, the resonances coincide with the natural frequencies of the beam satisfying clamped-free boundary conditions applied at either end—the clamped-free natural frequencies satisfy (**78**, **87**)

$$\cos\hat{\beta}\sqrt{\Omega}\hat{\ell} + \operatorname{sech}\hat{\beta}\sqrt{\Omega}\hat{\ell} = 0. \tag{5.2}$$

When the plate is thinner than the beam, we observe that the resonances shift to coincide with the natural frequencies of the pinned-free beam, where Ω satisfies (**87**)

$$\sin\hat{\beta}\sqrt{\Omega}\hat{\ell} - \cos\hat{\beta}\sqrt{\Omega}\hat{\ell}\tanh\hat{\beta}\sqrt{\Omega}\hat{\ell} = 0. \tag{5.3}$$

The roots arising from equation (5.2) coincide with the denominator terms of $\mathbf{M}$ and $\mathbf{V}$, hence when approaching a resonance from (5.2), terms within (D.2) or (4.18) will become large and cause poorly conditioned matrices. However, any matrix manipulations either involve computing the minimum norm least-squares solution or the solution to an algebraic eigenvalue problem; we find these methods to be sufficiently numerically stable for our needs even when the matrices are poorly conditioned—as corroborated by the observed shift in flexural resonances from (5.2) to (5.3), as in Figs 2–3, where our analytical solutions indeed match the FEM computations.

The boundary conditions applied on the beams (A.9) and (A.11) are the same regardless of relative thickness of the beam to the plate, and in both cases the source terms (2.2)–(2.4) are given by the same expressions with dependencies on both ϵ and h. The behaviour of the resonances produced by the system naturally shifts depending on the relative size of ϵ to h, to the cases (5.2) or (5.3); in any case, all components of displacements, rotations, forces and moments are conserved between the plate and the beams (at $\mathbf{x} = \mathbf{X}$ and $z = \frac{h}{2L}$). The behaviour of the beam is dependent upon the ratio of $\frac{\epsilon}{h}$ as to whether, at the base of the beams, displacements and rotations are dominant (as in the case of (5.2)) or displacements and moments are dominant (as in the case of (5.3)). This is consistent with (**103**, **105**), who considered the effect of the assumed continuity conditions on the resonances induced by beams atop an elastic half-space. Therein (**103**, **105**), unimodal solutions were compared with the asymptotic framework developed by (**103**, **106**) to consider the interaction between Rayleigh waves and resonant arrays atop the elastic media.

5.1 *Verification for one beam per primitive cell*

Referring to Figs 2 and 3, we observe that the branches from our eigensolutions match those provided by the 3D FEM computations, but slightly differ from case to case. From Fig. 2(a), we see the eigenmodes from Case 1 correspond to strongly perturbed flexural Kirchhoff–Love free-space modes, where the compressional resonances introduce large band gaps within the band structure. Comparing Case 1 to 2, we see $\mathbf{M}$ weakly perturbs the Case 1 eigenmodes and introduces narrow band gaps at resonance (5.2). Comparing Case 2 to 3, we see the addition of weakly perturbed 'light lines' corresponding to presence of dilational and shear waves now included in the system.

The effect observed by the flexural beam motion is regime dependent. For instance, clamped-free resonances (5.2) introduce very flat resonant bands which cut through any case 1 modes and create narrow bandgaps—as in Fig. 2(d) and Colquitt *et al*. (**78**). In such clamped-free regimes, the dispersive nature of the system is dominated by compressional beam motion and hence Case 1 provides sufficient accuracy provided one operates away from flexural resonances. As for pinned-free resonances (5.3), their presence introduces nearly flat bands which are not associated with the generation of bandgaps—as in Fig. 3(d) and (e). When the beams motion is in the pinned-free regime we observe only the first Case 1 branch is dominated by compressional beam motion, and for higher frequencies the flexural beam motion cannot be ignored. Moreover, in the pinned-free regime shown in Fig. 3, the FEM computations show that for frequencies higher than the Kirchhoff–Love 'light' lines torsional deformations within the beams become important, and our analytical solutions no longer match the FEM computations.

The error plot in Fig. 2(e) shows that, when torsional deformations within the beams can be neglected, the error of our analytical solution scales with ϵ^2—as expected since these terms are disregarded from our complementary coefficients (see Appendix B); the higher frequency eigenmode happens to be more accurate than the lower one due to the proximity of the flexural resonance affecting the condition numbers of our matrices. Lastly, as $\epsilon\Omega$ approaches unity, the asymptotics of the solution breakdown and are no longer valid.

Figure 4 compares the isofrequency contours (Case 2) to scattering simulations from the generalised Foldy solution (Case 3). We see that solutions from the closely related Green's functions (D.2) and (4.18) show one and the same solution—one over physical space and the other in reciprocal space. Additionally, when considering low frequency flexural modes propagating in the plate, Case 2 provides sufficient accuracy. In the following sections, we consider purely out-of-plane incident sources and operate at low frequencies such that Case 2 eigensolutions (D.2) or scattering solutions (4.18) provide sufficient accuracy.

5.2 *Multiple beams per primitive cell*

Extending the eigenvalue problem (D.2) to consider any P beams per primitive cell is straightforward, by modifying (3.9)–(3.11) to sum over the contribution from each beam in the cell. Additionally, one considers (3.14), (3.18)–(3.21) in the limit as $r_{1J} \to 0$ for every $J = 1, \ldots, P$; these asymptotic expressions remain unchanged, other than reinstating indices, since the Jth object is assumed dominant as $r_{1J} \to 0$. Figure 5 shows that our scheme, from (D.2) Case 2, is capable of determining the dispersion relations for systems containing multiple beams per cell—the comparison to the FEM dispersion curves is excellent beneath 50 Hz. Above this frequency, observe the branches from (D.2) start to deviate from the correct values due to the asymptotics breaking down.

6. Deep-subwavelength topologically protected states

Broken degeneracies produce states either classed as topologically trivial or non-trivial, depending on whether the initial degeneracy was induced trivially, solely because of the underlying lattice, or induced from non-trivial spacial symmetries within primitive cells. For instance, the topologically trivial edge states considered by Torrent *et al*. (**25**) are induced from breaking a trivial degeneracy through the introduction of resonance.

In this section, we design topologically non-trivial states arising from deliberate broken symmetries within primitive cells. Our precise approach follows that of valleytronics, where we

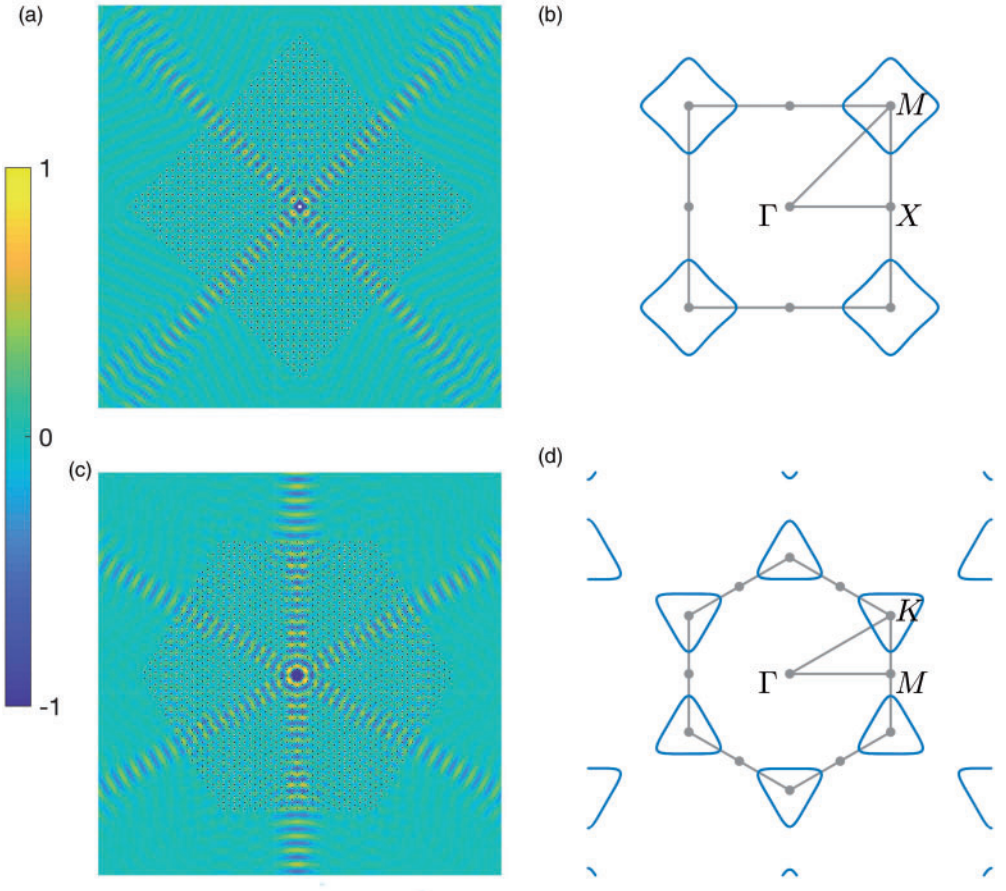

Fig. 4 Comparisons between isofrequency contours computed from (D.2) Case 2 and our generalised Foldy solution (4.18) Case 3. (a) and (b) take the parameters from Fig. 2, the isofrequency contours and scattering simulations were calculated at $\Omega = 9$ ($\omega = 221.0287$ Hz) for a purely out-of-plane monopole incident source, setting $\varpi_{\text{inc}} = 1$ within (4.4). (c) and (d) are identical to (a) and (b), other than setting $\boldsymbol{\alpha}_1 = \cos(\frac{\pi}{6})\mathbf{e}_x + \sin(\frac{\pi}{6})\mathbf{e}_y$ and $\Omega = 7.5$ ($\omega = 184.1906$ Hz). The colour bar refers to the normalised real parts of the total out-of-plane displacement field of the plate within (a) and (c), where the location of beams is shown by the small black dots. The first and irreducible Brillouin zone are plotted in grey in (b) and (d).

purposefully break symmetry induced Dirac cones leaving behind pairs of time-reversal-symmetry related valleys. These valleys, or band-structures with locally quadratic curvature surrounding a topologically non-trivial bandgap, produce topological vortex states (**107**) which undergo a topological phase transition from beneath to above such a bandgap. This transition provides the valley states with a corresponding pseudospin of opposite chirality, which produces efficient 'conduction', or energy propagation, along the interfaces or edges thus generating the topologically protected interfacial or edge states (**108**). The generation of these topologically protected states

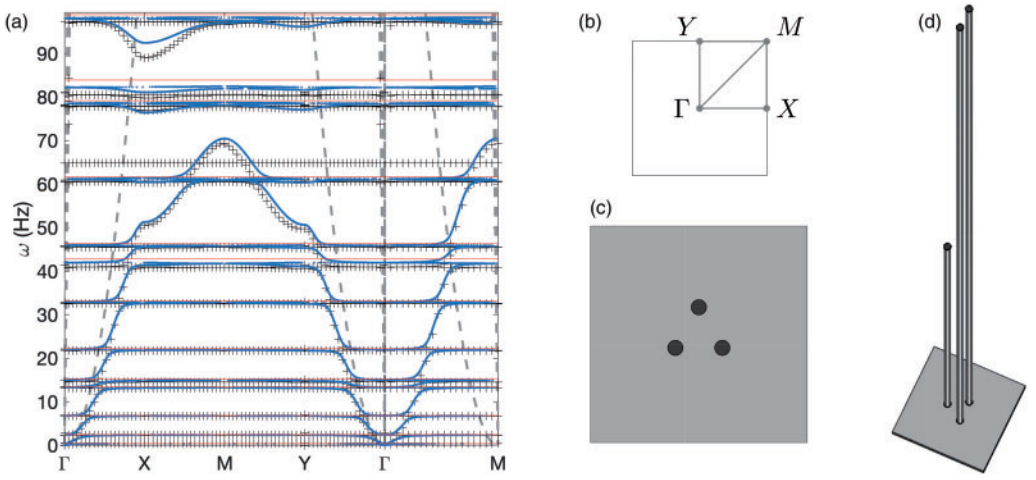

Fig. 5 Comparisons of the dispersion curves, in (a), computed from the eigenvalue problem (D.2) Case 2 (blue dots) and FEM computations (black crosses); here, the fundamental cell is shown in (c) (top view) and (d) (side view) where $h = 0.05$ m and the dimensionless parameters (again scaled with L) are $\boldsymbol{\alpha}_1 = \mathbf{e}_x$, $\boldsymbol{\alpha}_2 = \mathbf{e}_y$, $\mathbf{X}_{1J} = 0.125\left[\cos(\frac{2\pi(J-1)}{3} + \frac{\pi}{2})\mathbf{e}_x + \sin(\frac{2\pi(J-1)}{3} + \frac{\pi}{2})\mathbf{e}_y\right]$, $\hat{\ell}_{11} = 4.50$, $\hat{\ell}_{12} = \hat{\ell}_{13} = 11.25$, $\epsilon_{1J} = 0.035$, for $J = 1, 2, 3$. Here, we plot $\omega = \omega(\boldsymbol{\kappa})$ throughout the irreducible Brillouin zone (b). The green and red lines correspond to the resonances from (5.1) (higher frequency) and (5.2), respectively.

within the topological bulk bandgaps is related to the QVHE, and is demonstrated pictorially in Fig. 2 of (**6**). These topologically non-trivial modes correspond to interfacial (**8**, **42**, **79**, **109**) and edge (**24**, **110**–**112**) states with strong localisation and robustness due to the topological protection.

Topological quantities such as the Chern number or Berry curvature (**44**, **68**) characterise the direction of such vortex states, and can be used to identify the topological phase transition which occurs between the lower and upper valleys of a symmetry broken degeneracy (**44**). Suitably engineered chiral-mirrored pairs, as shown in Fig. 6(a) and (c), also undergo a topological phase transition and have chiral-mirrored Berry curvatures and hence chiral-mirrored vortex states. Placing two such media together, as in Fig. 6(b) and (d) results in interfaces in which Berry curvatures of opposite sign overlap. Consequently, topologically protected interfacial states emerge (**72**, **113**). These valley Hall edge states are known as Zero Line Modes (ZLMs).

Chiral induced interfacial states can be created without the use of topology, by breaking time-reversal-symmetry. However, active methods are required in a phononic setting. For instance, Carta *et al*. (**79**, **80**) consider gyro-topped beams affixed to elastic plates and demonstrate robust one-way interfacial states between media with counter-rotating chiral flux. Wang *et al*. (**24**) melds the ideas surrounding topology and actively inducing chirality to consider a symmetry induced degeneracy actively broken, by gyricity, generating robust one-way edgestates. Within photonics, externally applied magnetic fields allow time-reversal-symmetry to be passively broken to generate states with a single chirality, as in (**26**, **27**, **114**, **115**).

Our topologically non-trivial states exist passively and are not restricted to one-way propagation. Our symmetry protected Dirac cones coalesce with the flexural resonances of the constituent

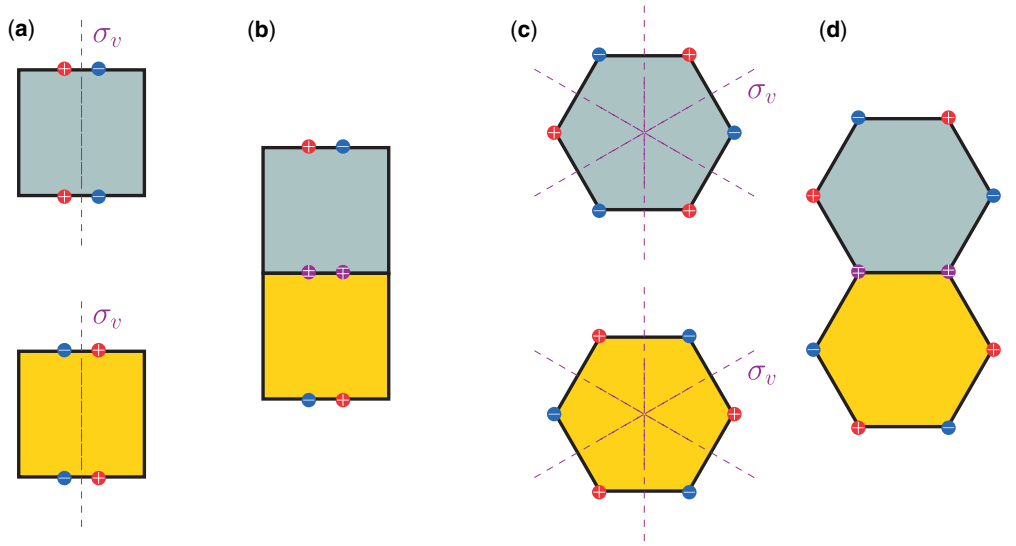

Fig. 6 The associated Berry curvature from σ_v symmetry breaking for chiral-mirrored pairs of primitive cells (**68**, **70**). Here, grey and yellow cells represent any chiral-mirrored primitive cell pairs, derived from perturbations which break the σ_v symmetries contained within the unperturbed cells; the vertical σ_v symmetries are plotted by the purple dashed lines for square and hexagonal lattices in (a) and (c), respectively. Exemplar sign Berry curvatures, for the bands bounding any symmetry-protected gapped degeneracy (by σ_v breaking), are denoted ⊕ and ⊖ referring to locations with opposite (non-zero) sign in Berry curvature. (b) and (d) show how the Berry curvature interacts when two such chiral-mirrored pairs are joined at an interface, where ⊕ and ⊖ denote locations at which ⊕ and ⊖ overlap, creating the topologically protected interfacial states known as zero line modes.

beams, and hence can be tuned to a required frequency by simply changing the parameters of the beams; moreover, they can be tuned into a deep-subwavelength regime, to frequencies far lower than traditional Bragg scattering (**63**). However, the near-resonant degeneracies lie on flat bands corresponding to slow sound within the wave spectrum; once these degeneracies are broken, they result in narrow-band energy gaps which still generate topologically non-trivial states. Additional graded rainbow (**116**) effects could be applied to increase the effective band gap of the media.

The polynomial eigenvalue problem (3.23) is formed from Hermitian matrices; subsequently (**117**), we expect bands to vary continuously unless approaching a degeneracy. Our focus is on vertical σ_v symmetries for triangular arrangements of beams in both square and hexagonal primitive cells, which induce symmetry protected degeneracies along the XM path in square lattices (**70**) and are guaranteed at the KK' high symmetry points in hexagonal lattices (**6**, **40**)—provided the structure in physical space has the σ_v symmetries shown in Fig. 6. Breaking the σ_v symmetries gaps such degeneracies and leads to the QVHE.

These chiral states exist because of the topological properties derived from the bulk (**118**, **119**). One could consider the bulk-boundary (or bulk-edge) correspondence (**120**, **121**) applicable to interfaces or edges, between two distinct bulk media, provided (**68**) opposite sign topological quantities are not projected onto the same point (and hence the bulk-boundary correspondence

cannot account for the creation of ZLMs as given in Fig. 6). In such cases, the bulk-boundary correspondence correlates non-zero Chern numbers (and hence Berry curvature) to the existence of topologically protected interfacial and edge states.

The works of Ochiai (**118**, **122**, **123**), Ochiai *et al.* (**110**) and Yao *et al.* (**124**) remark that edges, between a media with topologically induced chiral states and the free space, will inherit the non-trivial topological properties of the bulk media. Provided modes cannot propagate into the surrounding free-space, they can be localised by one-sided chiral flux (**118**) and give rise to topologically non-trivial edgestates. Our edgestates only occur when non-zero Berry curvature meets the free space and hence are produced in accordance with the bulk-edge correspondence. These edgestates are shown to be sufficiently robust to navigate corners, unless corner states exist which readily shed energy into the free space.

Within a photonic setting (**110**, **118**), physical intuition of the surrounding free space is important regarding the creation of edgemodes. For instance in (**118**), the case of photons in air was considered and operating above the light line to induce leaky waves was necessary to confine energy propagation along edges, since energy of the photon propagating in the crystal was higher than the 'vacuum level' in the free space (air). Otherwise, only the conservation (**33**) of $\kappa_{\|}$, denoting the component of the wavevector parallel to the surface of the crystal, is crucial to determine the group velocity of waves conserved at such an edge, and whether propagation is allowed within the free space—as in Fig. 4 (or in a photonic setting (**62**, **110**)). Here, we operate at the subwavelength scale far beneath the analogous light lines and expect the near-resonant behaviour responsible for these subwavelength states to confine energy to the edge of the crystal, as in (**41**). We investigate these edgemodes in a similar fashion to Torrent *et al*. (**25**), where we consider ribbon strips containing edges of interest but confirm the confinement of states along the $\Omega = \Omega(\kappa_{\|})$ branches by visualising the edgemodes.

The creation of these topologically nontrivial states requires simple arguments based upon group theory (**125**, **126**) in a periodic setting (**127**, **128**), in which we can infer which bands are symmetry induced and hence which degeneracies have non-trivial symmetry protection. We denote $G_{\boldsymbol{\kappa}}$ to be the point group symmetry[2] of a cell in reciprocal space at $\boldsymbol{\kappa}$, and remark that any eigenfunction can be used for an irreducible representation of $G_{\boldsymbol{\kappa}}$ (**128**). A fitting choice of eigenfunction would be the eigenmode corresponding to $\boldsymbol{\kappa}$, that is, the eigenstate (**70**) corresponding to fixed Bloch momentum vector $\boldsymbol{\kappa}$.

As with dispersion, we expect our eigenmodes to continuously vary unless we approach dispersionless crossings; classifying eigenmodes by symmetry allows one to infer which bands are symmetry induced and which bands are allowed to cross, and hence form degeneracies. Typically this is done at the high symmetry points. However, one can apply compatibility relations (see Fig. 3.7 and Table 3.10 in (**128**) for hexagonal lattices, and Fig. 34 and Table 26 in (**127**) for square lattices) to relate irreducible relations for $\boldsymbol{\kappa}$ along XM or ΓK, for instance, to those at the high symmetry points in $\boldsymbol{\kappa}$ space and vice versa. Note, only G_{Γ} has the full point group symmetry of the lattice and $G_{\boldsymbol{\kappa}\neq\mathbf{0}} \leq G_{\Gamma}$—that is to say $G_{\boldsymbol{\kappa}\neq\mathbf{0}}$ is a subgroup of G_{Γ}.

Therefore, symmetry induced degeneracies can be identified by analysing the parity of eigenmodes immediately surrounding such a crossing along the irreducible Brillouin zone; since eigenvalues are not degenerate away from any crossing, one obtains information about the parity of branches and whether the dispersionless crossings are indeed symmetry protected and hence simple to gap. A telling sign that bands are symmetry induced is that the irreducible representations match

[2] For a formal definition of $G_{\boldsymbol{\kappa}}$ within hexagonal or square lattices refer to (**40**) or (**117**), respectively.

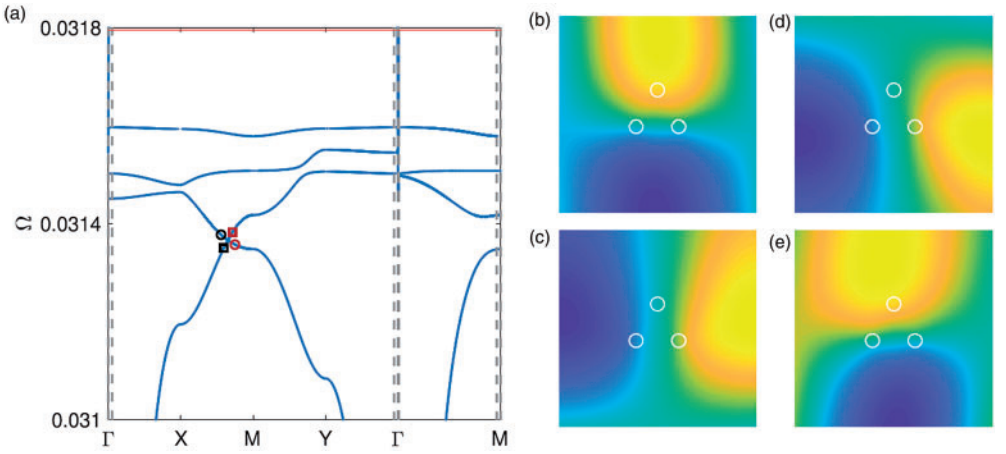

Fig. 7 The Dirac point, in (a), observed by zooming in about the first flexural resonance from Fig. 5(a). Here, we plot the dimensionless dispersion curves $\Omega = \Omega(\boldsymbol{\kappa})$ from our eigenvalue problem (D.2), the red line corresponds to the lowest flexural resonance satisfying (5.2). The dimensional frequency of the Dirac point in (a) is $\omega = 0.38516$ Hz, the FEM computed result is $\omega = 0.38127$ Hz, hence our results agree with a relative error of 1.02% . (b), (c), (d) and (e) show the eigenmodes at the respective points ◯, □, □ and ◯ from the bands in (a), where the real part of the out-of-plane displacement fields are plotted in (b)–(e).

the basis functions of the irreducible representations within the appropriate character tables. We proceed by designing structured media in which we expect symmetry protected degeneracies to occur and confirm this behaviour by comparing the eigenmodes in the vicinity of such a degeneracy to the character tables. Subsequently, by simply breaking the symmetries within the cell, we gap such degeneracies and create topologically non-trivial states; these subwavelength states will be topologically protected, the robustness of which will be demonstrated in a number of scattering simulations.

6.1 *Robust deep-subwavelength topological waveguides within square arrays*

Consider the square primitive cell in Fig. 5(c) which has one vertical σ_v reflectional symmetry and hence the required symmetries within Fig. 6(a). We denote $\boldsymbol{\kappa}_{XM}$ to be any $\boldsymbol{\kappa}$ along XM, and note σ_v allows accidental degeneracies to occur for some $\boldsymbol{\kappa}_{XM}$ (**68**). Zooming in on the first resonance of Fig. 5(a), as shown in Fig. 7(a), we see such a dispersionless crossing. In (**70**), it was shown that the irreducible representations along $\boldsymbol{\kappa}_{XM}$ are compatible with those at G_X and hence (**128**) the assignment of symmetry for G_X is deduced by looking at any $G_{\boldsymbol{\kappa}_{XM}}$, and vice versa.

Consider the eigenmodes in Fig. 7(b), (c), (d) and (e) corresponding to Fig. 7(a) points ◯, □, □ and ◯. The states here match the linear basis functions of the irreducible representations in table 2; the eigenmodes ◯ and ◯ match the y or linear B_2 basis. Additionally, □ and □ match the x or linear B_1 basis. Therefore, applying the above compatibility condition, we do indeed deduce $G_X = C_{2v}$. Moreover, since $G_X \leq G_\Gamma$, then $G_\Gamma = C_{2v}$ is immediately confirmed. Further application of the compatibility relations along $\boldsymbol{\kappa}_{XM}$ ensures the band following □ and □ will have irreducible representations corresponding to the B_1 basis and hence is odd about the direction following the

Table 2 Excerpt of the C_{2v} character table—we require only the linear basis functions spanning the irreducible representations (IRs).

	Classes				
IRs	E	C_2	σ_v	σ_h	Basis
B_1	$+1$	-1	$+1$	-1	x
B_2	$+1$	-1	-1	$+1$	y

Bloch momentum vector $\boldsymbol{\kappa}_{XM}$ in which the states exists. Similarly, the band following ◯ and ◯ will have irreducible representations corresponding to the B_2 basis, and be even about the $\boldsymbol{\kappa}_{XM}$ direction. Such a well ordered and opposite parity of branches, with irreducible representations of correct symmetry basis, allows the $\boldsymbol{\kappa}_{XM}$ crossing to exist and confirms its symmetry protected nature.

We perturb the primitive cell in Fig. 5(c) by positively and negatively rotating the arrangement of beams to create the cells in Fig. 8(b) and (c). The σ_v symmetry breaking reduces the symmetry set from $\{G_\Gamma, G_X\} = \{C_{2v}, C_{2v}\}$ in cell Fig. 5(c), to $\{G_\Gamma, G_X\} = \{C_2, C_2\}$ in cells Fig. 8(b) and (c); the perturbation affects the well ordered states along branches in Fig. 5(a) by mixing the parity of states along the branches. Subsequently, the first and second bands find themselves repulsed and the symmetry induced degeneracy is broken to form the subwavelength topologically non-trivial band gap in Fig. 8. By stacking chiral-mirrored pairs of such structured media, as in Fig. 8, we observe the QVHE, in which we are guaranteed the creation of ZLMs by the mechanism presented in Fig. 6(b). Indeed, Fig. 8(d) and (f) show the familiar even and odd parity ZLMs localised to two distinct interfaces, generated by the sole σ_v symmetry breaking within the square cell—as in (**68**, **70**).

Consider Fig. 9 in which we test the designs of two phononic crystals (a) and (c) with different edges, formed from tessellating the ribbon media in Fig. 8(d). Note, from Fig. 6(a), the edges of Fig. 9(a) have sections of non-zero Berry curvature meeting the surrounding free-space and hence, by the bulk-edge correspondence, we expect the existence of topologically protected edgestates. However, the edges of Fig. 9(c) have negligible Berry curvature and hence cannot support chiral states. We consider a monopole point source, whose frequency lives within the bulk bandgap. Placing this source as shown in Fig. 9(a) and (c), the scattering computations of Fig. 9 (b) and (d) indeed show the excited ZLM which resembles the eigenstates within Fig. 8(d) and (e); moreover, these scattering computations confirm our predictions regarding the existence of protected edgestates by the bulk-edge correspondence.

The ribbon eigenmodal analysis in Fig. 9(e)–(h) clearly shows the existence of edgemodes living within the topologically non-trivial band gap of Fig. 8(a). Those in Fig. 9(e) and (f) satisfy the bulk-edge correspondence and hence inherit topological protection from the structured bulk media and show similar decay as the ZLMs in Fig. 8 (d)—these modes are sufficiently robust to efficiently propagate around the edges of Fig. 9(a); they exist far beneath the analogous light line and are heavily localised to the edge. The preferential direction observed in Fig. 9(b) is due to the anisotropic dipole nature of the scatterers, as expected at the near flexural resonances of the constituent beams.

Figure 9(b) clearly show efficient mode conversion between the interfacial Fig. 8(d) states and edge Fig. 9(e) states, where the absence of backscatter of energy at the corners of the designs is attributed to topological protection. The only energy losses observed here are due to the presence of sharp corners, in Fig. 9(a), which readily produce corner states (**43**–**45**) and shed energy into the

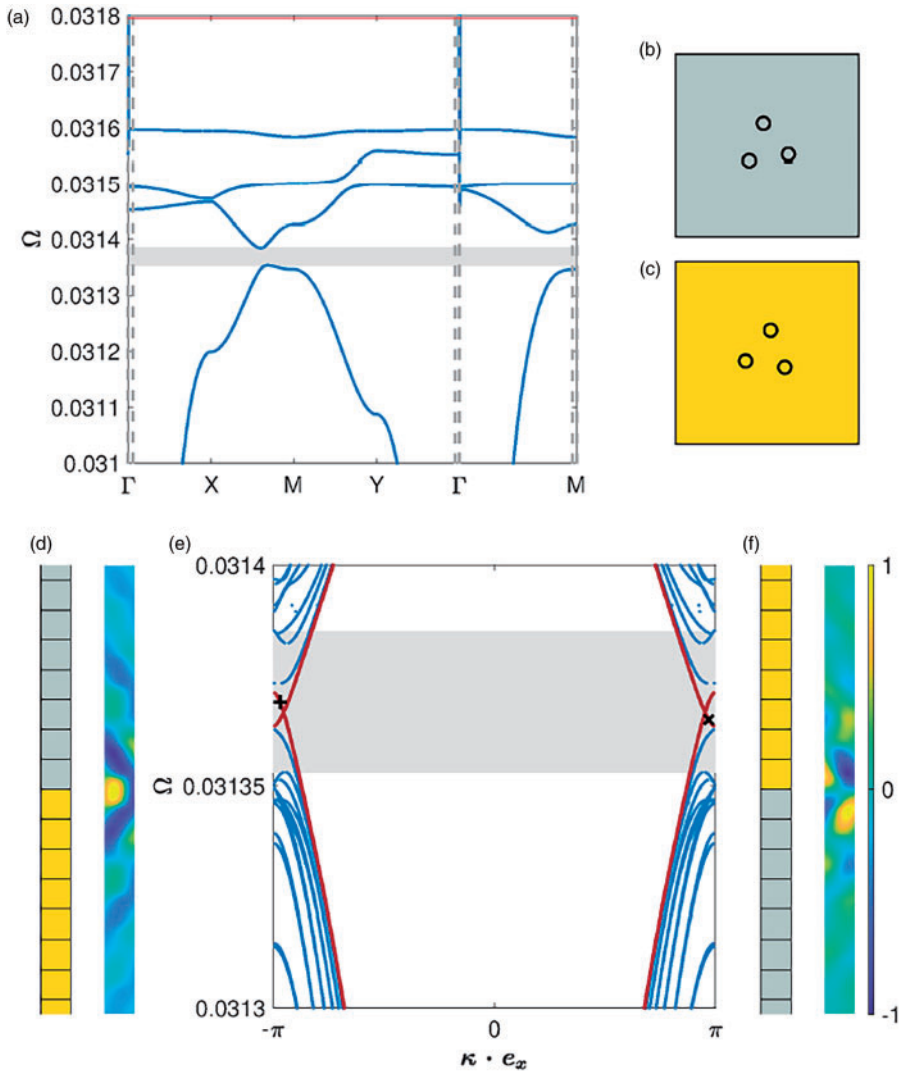

Fig. 8 (a) shows the Floquet-Bloch dispersion branches of the primitive cell in (b). Cells (b) and (c) are obtained by perturbing the arrangement in Fig. 5(c) via rotations of θ'. By setting $\mathbf{X}_{1J} = 0.125\left[\cos(\frac{2\pi(J-1)}{3} + \frac{\pi}{2} + \theta')\mathbf{e}_x + \sin(\frac{2\pi(J-1)}{3} + \frac{\pi}{2} + \theta')\mathbf{e}_y\right]$, the grey (b) and yellow (c) cells, respectively correspond to positive and negative rotations in which $\theta' = \pm\frac{\pi}{20}$. The topological band gap is shaded in grey in (a). (d) and (f) show ribbon media, formed by stacking the chiral pairs in (b) and (c) as shown. The dispersion curves of these ribbon media, obtained from our Floquet–Bloch analysis (D.2), are plotted in (e) where the bulk band gap from (a) is also highlighted in (e). The interfacial modes of interest are plotted in red in (e), the even (d) and odd (f) interfacial states are plotted next to the ribbon media in which they persist; the eigenstates in (d) and (f) correspond to the points + and × in (e), respectively.

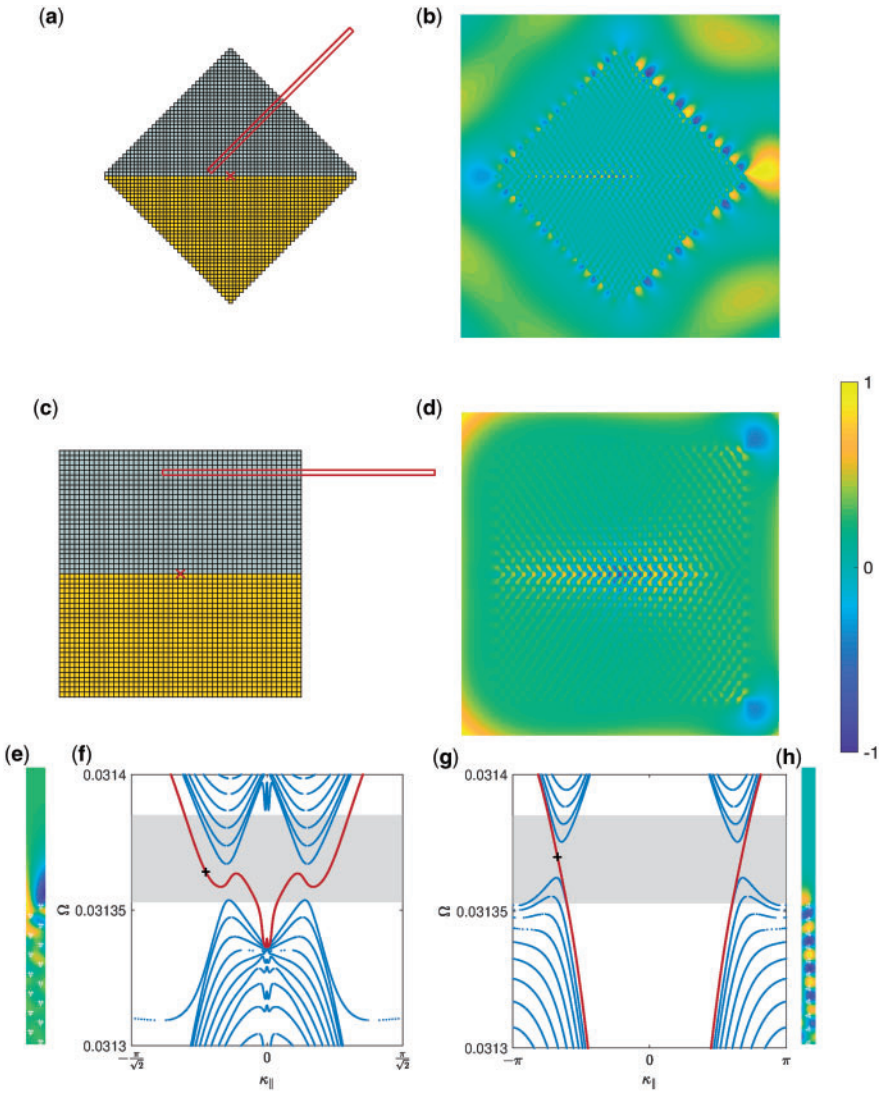

Fig. 9 Generalised Foldy simulations (b) and (d) for the phononic crystal designs respectively shown in the schematics of (a) and (c); both (a) and (c) are formed from 2450 cells, half grey and half yellow cells from Fig. 8(b) and (c), for a total of 7350 beams atop an elastic plate of infinite expanse. The incident sources, in (b) and (d), both consider monopoles with $\varpi_{\text{inc}} = 1$ from (4.4) and $\mathbf{X}_{\text{inc}}$ is marked by × in (a) and (c). The frequencies of the point-sources both lie within the topological band gap of Fig. 8 (a), and are set to $\Omega = 0.0313695$ for (b) and $\Omega = 0.0313698$ for (d). The red rectangular strips in schematics (a) and (c) represent ribbon strips, half over the bare plate and half over the grey medium—(f) and (g) show the dispersion curves taken by considering Floquet–Bloch boundary conditions (from (D.2)) on the edges of these strips, the edge modes of interest are plotted in red and the bulk band gap is again highlighted in grey from Fig. 8(a). Here, $\kappa_\parallel$ denotes the component of the wavevector parallel to the surface of the crystal. (e) and (h) correspond to eigenmodes from + within panels (f) and (g), respectively, where the locations of the beams are shown by white crosses. The colour bar refers to the normalised displacement fields of (b), (d), (e) and (h), where the real part of the out-of-plane displacement field has been plotted.

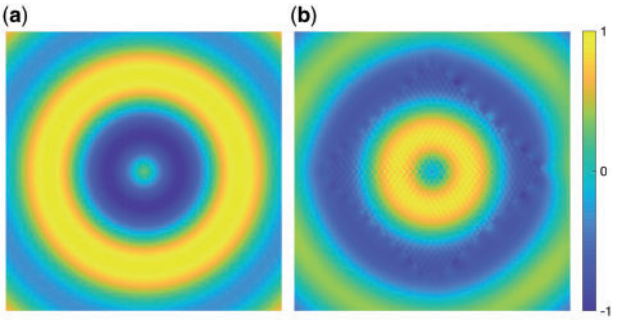

Fig. 10 Comparisons of the incident field (a) and scattered field (b), the addition of which yields the total field of Fig. 9(b). The incident source was set to $\varpi_{\text{inc}} = 1$ from (4.4) and $\mathbf{X}_{\text{inc}}$ is marked by × in Fig. 9(a). The colour bar shows the real part for the normalised wavefields.

free space. We suspect the superior topological protection arising from the non-zero Berry curvature in the hexagonal case, Fig. 6(c), will ensure a greater efficiency of the propagation between ZLMs and edgestates by forbidding corner states. The eigenmodes in Fig. 9(g) and (h) do not benefit from topological protection. The lack of chiral-flux means they slowly decay within the non-trivial bulk and are only weakly excited in the scattering simulations of Fig. 9(d), where again we observe the presence of corner states.

The low-frequency, long-wavelength regime within which our designs manipulate the propagation of waves should not be understated. Refer to Fig. 10 comparing the incident (4.5) and scattered field; here, the incident source is of wavelength 30–40 times that of the lattice spacing. Observe how the respective peaks and troughs from the incident field align with the troughs and peaks in the scattered field, the addition of which yields the total field from Fig. 9(b).

6.2 *Superior topological protection: subwavelength states in hexagonal arrays*

The symmetry arguments in section 6.1, underpinning the creation of topologically protected states in square lattices also apply to hexagonal lattices, where the degeneracies now occur at the KK' high symmetry points. In the hexagonal case, larger band gaps can be produced as larger rotations, through θ', allow valleys to retain their locally quadratic behaviour in the vicinity of KK'. The pros and cons of different geometrically designed interfacial states for square and hexagonal lattices are summarised in Fig. 12 of (**68**).

The hexagonal primitive cell in Fig. 11(c) has $3\sigma_v$ spatial symmetries which induce protected degeneracies at the KK' locations of the first Brillouin zone, provided $\{G_\Gamma, G_{K,K'}\} = \{C_{3v}, C_{3v}\}$ (**6**, **40**). Here $C_{3v} = C_3 + 3\sigma_V$ and $G_{K,K'}$ represents $G_{\boldsymbol{\kappa}}$ at the K and K' high symmetry points. Figure 11(e) and (f) respectively correspond to the eigenstates at points ◯ and □ in Fig. 11(a), observe the eigenmodes □ and ◯ respectively match the E basis functions x and y from the C_{3v} character Table 3. The states at Fig. 11(a) □ and ◯ exist on the dispersionless sections approaching the crossing at K and hence are compatible with G_K, and by time-reversal-symmetry $G_{K'}$—therefore $G_{K,K'} = C_{3v}$. It follows $G_\Gamma = C_{3v}$, indeed since $G_K \leq G_\Gamma$.

Furthermore, applying the compatibility relations within Sakoda (**128**), we confirm the band following Fig. 11(a) points ◯ & ◯ also has irreducible representations corresponding to the E

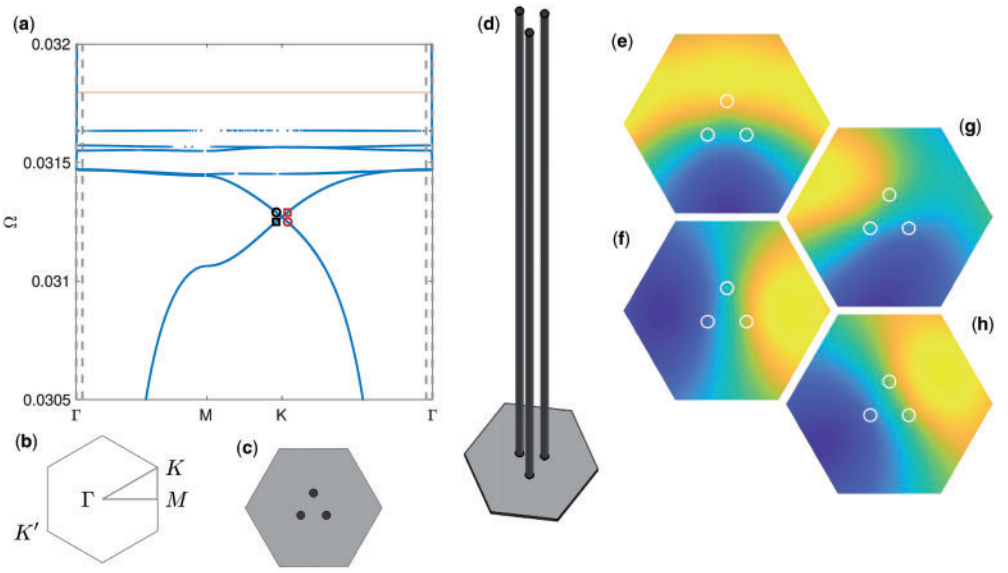

Fig. 11 The same as Fig. 7, but with $\boldsymbol{\alpha}_1 = \cos(\frac{\pi}{6})\mathbf{e}_x + \sin(\frac{\pi}{6})\mathbf{e}_y$ and $\hat{\ell}_{11} = \hat{\ell}_{12} = \hat{\ell}_{13} = 11.25$. Here, (a) we plot the dimensionless dispersion curves $\Omega = \Omega(\boldsymbol{\kappa})$ from our eigenvalue problem (D.2) throughout the irreducible Brillouin zone (b), appropriate for the fundamental cell given in (c) (top view) and (d) (side view). (e), (f), (g) and (h) show the eigenmodes from ◯, □, □ and ◯ in (a) respectively, where the real part of the out-of-plane displacement is plotted in (e)–(h). Here the dimensional frequency of the Dirac point is 0.38398 Hz, and we expect a similar relative error as in Fig. 7.

Table 3 Excerpt of the C_{3v} character table; only the linear basis functions spanning the irreducible representations (IRs) are required

	Classes			
IRs	E	$2C_3$	$3\sigma_v$	Basis
E	+2	−1	0	$\{x, y\}$

basis and is even with respect to the symmetry line following the Bloch momentum wave vector, $\boldsymbol{\kappa}$, defining each state. Similarly, the states along the band following □ & □ are odd and match the E basis. Therefore, the well ordered and opposite parity eigenmodes, with the correct symmetry along branches, allows the crossing to exist at K and confirms its symmetry protected nature.

Similarly to section 6.1, we rotate the arrangement of beams in Fig. 11(c) to reduce the symmetry set: from $\{G_\Gamma, G_{K,K'}\} = \{C_{3v}, C_{3v}\}$ to $\{G_\Gamma, G_{K,K'}\} = \{C_3, C_3\}$ in Fig. 12(b) and (c) by σ_v symmetry breaking. Again, the perturbation affects the well ordered parities of eigenstates along the branches near the crossing, causing band repulsion and gapping the KK' Dirac points, as seen in Fig. 12(a). Observe the creation of ZLMs within Fig. 12(d) and (f), as described in Fig. 6(d). Furthermore, when

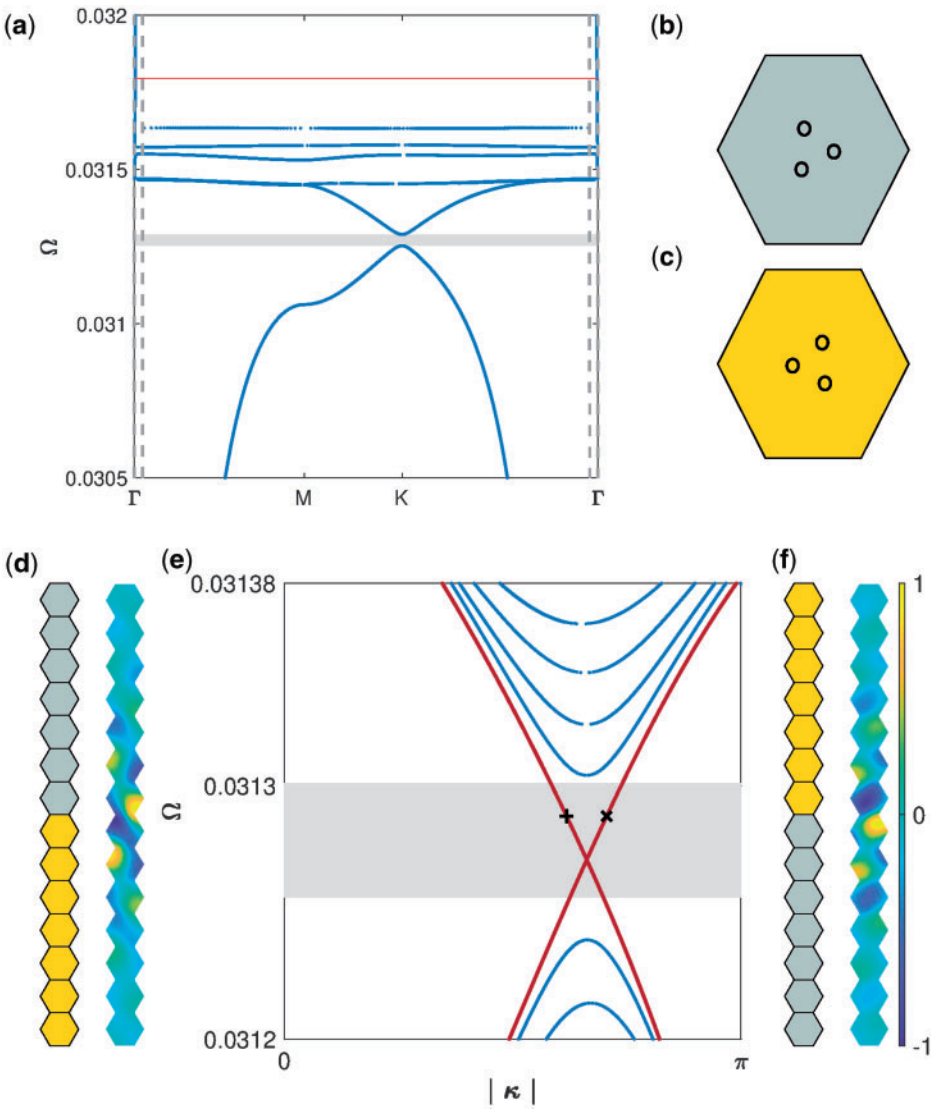

Fig. 12 The Floquet–Bloch dispersion curves (a) from the primitive cell (b). Cells (b) and (c) are obtained by perturbing the arrangement shown in Fig. 11(c) via rotations of θ'. By setting $\mathbf{X}_{1J} = 0.125\left[\cos(\frac{2\pi(J-1)}{3} + \frac{\pi}{2} + \theta')\mathbf{e}_x + \sin(\frac{2\pi(J-1)}{3} + \frac{\pi}{2} + \theta')\mathbf{e}_y\right]$, the grey (b) and yellow (c) cells, respectively correspond to positive and negative rotations by setting $\theta' = \pm\frac{\pi}{7}$. The topological band gap is shaded in grey in (a). (d) and (f) show ribbon media, formed by stacking the cells in (b) and (c) as shown. The dispersion relations of these ribbon media, from our Floquet–Bloch analysis (D.2), are plotted in (e) where the band gap from (a) is similarly shaded in (e). The interfacial modes of interest are plotted in red in (e), the even (d) and odd (f) ZLMs are plotted next to the ribbon media in which they persist; the eigenstates in (d) and (f) correspond to the points + and × in (e), respectively.

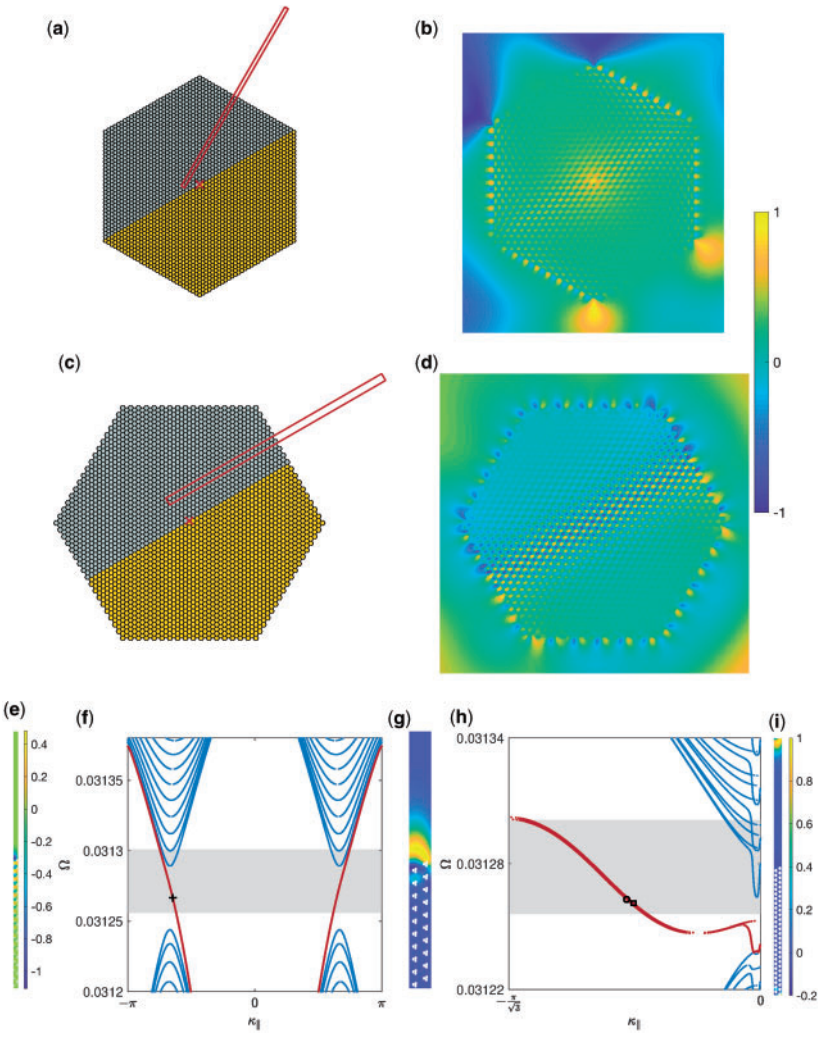

Fig. 13 Generalised Foldy simulations (b) and (d) for the phononic crystal designs, respectively shown in the schematics of (a) and (c); here (a) and (c) are respectively formed from 2611 and 2653 cells, with (nearly) half grey and half yellow cells from Fig. 12(b) and (c)—for a total of 7833 and 7959 beams atop an elastic plate of infinite expanse. The incident sources, in (b) and (d), consider monopoles with $\varpi_{\text{inc}} = 1$ from (4.4) and $\mathbf{X}_{\text{inc}}$ is marked by × in (a) and (c). The frequencies of the point-sources both lie within the band gaps from Fig. 12(a), and are set to $\Omega = 0.0312587$ for (b) and $\Omega = 0.0312852$ for (d). The red rectangular strips in schematics (a) and (c) represent ribbon strips, half over the bare plate and half over the grey medium; (f) and (h) show the dispersion curves taken by considering Floquet-Bloch boundary conditions (from (D.2)) on the edges of these strips. The edge modes of interest are plotted in red and the bulk band gap for the constituent cells is again highlighted in grey from Fig. 12(a). (e) corresponds to the eigenmode at + within (f). Similarly (g) and (i), respectively correspond to eigenmodes from points ◯ (on left-most branch) and □ (on right-most branch) in (h). The locations of the beams are shown by white circles in (e), (g) and (i). The colour bars refer to the normalised displacement fields of the computations they are next to, where the real part of the out-of-plane displacement field has been plotted. (b), (d) share the same colour bar. Also (g) and (i) share the same colour bar.

breaking $3\sigma_v$ symmetries within a hexagonal lattice we expect (**6**, **68**) even and odd ZLMs existing over two distinct interfaces, as observed in Fig. 12(d) and (f)—now following the ΓK direction of $\boldsymbol{\kappa}$.

There are two types of interfaces which can be constructed by tessellations of hexagonal cells, that is, zigzag or armchair interfaces. The zigzag interfaces are preferred for the construction of ZLMs since they offer greater topological protection (**8**). Figure 13(a) and (c) show two phononic crystals, both with zigzag interfaces supporting ZLMs, with zigzag (a) or armchair (c) edges. In contrast to square lattice, Fig. 9, the topologically non-trivial bulk derived from hexagonal primitive cells meeting the free-space always produces edges with non-zero berry curvature—as in Fig. 6(c). Therefore, by the bulk-edge correspondence we expect topologically protected edgestates to exist for both of the designs within Fig. 13(a) and (c).

The eigenmodal analysis in Fig. 13(e)–(i) confirms the existence of these topologically non-trivial edgestates, where we see modes which decay rapidly into the topological bulk—localised by the existence of chiral flux by the QVHE. Again we operate far beneath the free-space 'light' lines and observe modes confined to the edges of the crystal. In contrast to the ZLMs, the armchair edgestates (in Fig. 13(g)–(i)) offer a greater topological protection than the zigzag edgestates (Fig. 13(e) and (f)); the armchair edge produces two modes existing along two distinct edges within the ribbon, with much flatter bands and eigenmodes with superior localisation of energy than the sole mode existing for the zigzag edge.

The topological protection of the ZLMs and edgestates is confirmed by the scattering simulations in Fig. 13(b) and (d). Both of which show the ZLMs corresponding to the interfacial states of Fig. 12(d), which efficiently allow navigation of energy at the junction between the interface and edges via modal conversion of states; the topological protection of which accounts for the efficiency of the conversion, around sharp corners, with negligible backscatter and strong localisation along the topological interfaces and edges within the phononic crystal. The two distinct edgemodes for a sole chirality in Fig. 13(g) and (i) readily couple into one another—as a consequence of their minimal Fourier separation (**8**) in Fig. 13(h)—therefore, these modes are expected to efficiently navigate around the corners of the perimeter of the phononic crystal in Fig. 13(c). In Fig. 13(d), we observe conversion between the ZLMs and edgestates, which efficiently propagate around the entire perimeter; hence, Fig. 13(c) is truly a sub-wavelength phononic circuit whose efficiency and robustness is guaranteed by topological protection.

The same cannot be said of the design in Fig. 13(a). The ZLMs and edgestates within the design are topologically protected, and energy similarly navigates the corners by converting between interfacial and edgestates, where backscatter is still protected against. However, since only one topological edgestate exists, the energy cannot propagate around the entire perimeter of the phononic crystal and must be shed at its vertices. This is observed in Fig. 13(b) where corner states shed energy into the free space.

When joining any edges of grey and yellow hexagonal cells together, it is always the case that locations of opposite Berry curvature are projected onto one another and ZLMs are generated—refer to Fig. 6(c). Therefore, we may modify the design of Fig. 13(c) to introduce a variety of acute and obtuse bends along the interfaces, to demonstrate the robustness of ZLMs by achieving topological mode steering (Fig. 14(a)) or energy splitting (Fig. 14(d)). Acute ($\frac{\pi}{3}$) and obtuse ($\frac{2\pi}{3}$) bends are respectively associated with model preservation and conversion. We now excite modes by placing our source at the edge of the phononic crystals. Consider Fig. 14(b), observe the ZLM of Fig. 12(d) is conserved and able to navigate the acute bends within Fig. 14(a). Within Fig. 14(e), observe the ZLM of Fig. 12(d) is excited, at × in Fig. 14(d), and is readily split three-ways; model

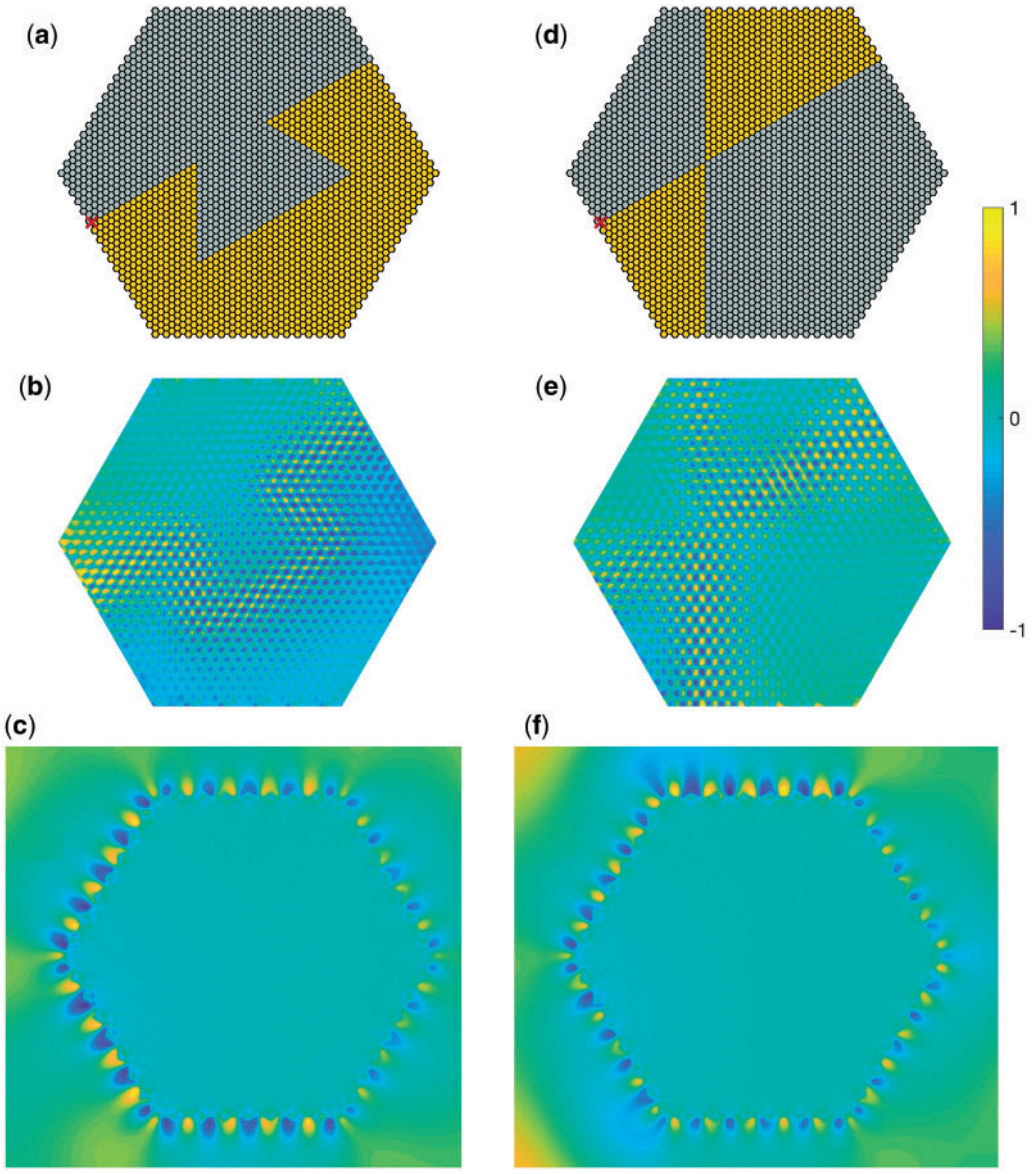

Fig. 14 Phononic crystal designs demonstrating ZLM steering and energy splitting in (a) and (d). Here, we modify the design of Fig. 13(c) to test the robustness of the ZLMs. (a) and (d) are both formed from 2653 cells with 1320 grey in (a) and 1826 grey in (d), for designs with a total of 7959 beams. The generalised Foldy simulations all consider monopole incident sources with $\varpi_{\text{inc}} = 1$ from (4.4) and $\mathbf{X}_{\text{inc}}$ is marked by × in (a) and (d); the frequencies of the sources all lie within the deep-subwavelength topological band gaps from Fig. 12(a), and are set to $\Omega = 0.0312816$ for (b), $\Omega = 0.0312692$ for (c), $\Omega = 0.0312826$ for (e) and $\Omega = 0.0312760$ for (f). The colour bar refers to the real part of the normalised displacement fields in all simulations.

conversion to the ZLM of Fig. 12(f) occurs at the $\frac{2\pi}{3}$ and π bends, and the ZLM of Fig. 12(d) is preserved at the $\frac{\pi}{3}$ bend. Note ZLMs are not always excited when operating within the topological band gap, the cases of Fig. 14(c) and (f) show this. Observe how the edgemodes in Fig. 13 (g)–(i) are excited in Fig. 14(a) and (d) at ×, and propagate around the entire perimeter of the phononic crystals. The topological mode steering and energy splitting occurs at the deep-subwavelength scale and in absence of backscatter, therefore demonstrating the robustness of modes.

7. Conclusion

Herein, we present our analytical solutions approximating dispersion and scattering from structured media built from arrays of elastic beams atop an elastic plate, appropriate for designing phononic crystals. The solutions are expressed through singular Green's functions, via evaluating Fourier series (for Floquet–Bloch bands) or Fourier transforms (for scattering from finite arrays) in the limits where they diverge. The problem is considerably simplified by the hypothesis of Euler–Bernoulli beam theory (**87**), which allows us to determine the forces and moments which couple into the plate from the constituent beams, and allows us to approximate the junction between the beams and plate as rigid disks. In sections 2.1 and 2.2, we show how to replace each beam with point monopoles and dipoles, whose coefficients determine forces and moments in terms of quantities defining arbitrary (finite) displacements and rotations, which encapsulate the assumed rigid portion of the plates motion.

In section 3, we show how to relate the singular Green's functions for the Fourier series and Fourier transform representations of solutions in the limit as they diverge, and how this allows one to cancel singularities from either side of the relation; allowing the construction of an eigenvalue problem determining the Floquet–Bloch dispersion branches from eigenvalues and eigenmodes from eigenvectors. In section 4, we apply Foldy's method to simulate scattering by a finite collection of beams under incidence. These solutions are tested against FEM computations in section 5, where they are found to be accurate, and reveal two regimes of motion for the beams—either flexing like clamped-free or pinned-free beams, depending on the ratio of the radius of beams to the thickness of the plate.

Finally in section 6, we apply our analytical solutions to consider topological arrangements of beams, again in good agreement with FEM computations, to form degeneracies with non-trivial symmetry protection. These degeneracies coincide with the first flexural resonance of the arrangements of the beams and hence can be tuned into a deep-subwavelength regime; additionally, they are simple to gap and produce the phononic analogue of the QVHE, where we demonstrate the existence of protected interfacial and edge states. These topologically protected interfacial and edge states coexist within the band gap of the bulk media. The interfacial states exist between two adjoining topological chiral-mirrored bulk media and correspond to ZLMs. The topological edgestates are formed in accordance with the bulk-edge correspondence, when one such topological chiral-mirrored bulk media meets the free-space. We build on this knowledge to design robust phononic circuits, where interfacial and edge states efficiently convert between one another and navigate corners, all in the presence of deep-subwavelength topological protection. This is further demonstrated by designing crystals which permit topological ZLM steering and energy splitting, again where topological protection prevents backscatter.

These demonstrations elucidate the creation of topological waveguides and energy splitters, at very low frequencies in a phononic setting, which could aid the creation of future seismic protection or energy harvesting devices to collect/mitigate vibrational energy. Similar examples have been

discussed in the context of phononics and photonics, where the idea of melding topology and resonance is quite general and promising in controlling waves in many physical settings, from Bragg to deep-subwavelength scales.

Acknowledgements

R.W. is thankful to Mehul P. Makwana for interesting discussions regarding topology and the QVHE. R. W. would also like to thank Daniel J. Colquitt for the intuition gained from discussing related problems (**78**, **79**). J.M.D.P. and R.V.C acknowledge the financial support from the H2020 FET-proactive project MetaVEH under grant agreement number 952039. R. W. appreciates funding from the EPSRC Centre for Doctoral Training in Fluid Dynamics across Scales, UK, reference EP/L016230/1. R.W. and R.V.C. also acknowledge funding from the, EU, H2020 project MetaVEH grant agreement number 952039.

References

1. R. Sepkhanov, Y. B. Bazaliy and C. Beenakker, Extremal transmission at the Dirac point of a photonic band structure, *Phys. Rev. A* **75** (2007) 063813.
2. X. Zhang and Z. Liu, Extremal transmission and beating effect of acoustic waves in two-dimensional sonic crystals, *Phys. Rev. Lett.* **101** (2008) 264303.
3. S. Bittner, B. Dietz, M. Miski-Oglu and A. Richter, Extremal transmission through a microwave photonic crystal and the observation of edge states in a rectangular Dirac billiard, *Phys. Rev. B* **85** (2012) 064301.
4. X. Huang, Y. Lai, Z. H. Hang, H. Zheng and C. T. Chan, Dirac cones induced by accidental degeneracy in photonic crystals and zero-refractive-index materials, *Nat. Mater.* **10** (2011) 582–586.
5. H. Guo, H. Liu, X. Zhang, H. Chen, W. Liu, S. Wang and Y. Cui, Dirac point and cloaking based on honeycomb lattice photonic crystal, *Appl. Phys. Express* **6** (2013) 042003.
6. M. Makwana, R. Wiltshaw, S. Guenneau and R. Craster, Hybrid topological guiding mechanisms for photonic crystal fibers, *Opt. Express* **28** (2020) 30871–30888.
7. L. Lu, J. D. Joannopoulos and M. Soljačić, Topological states in photonic systems, *Nat. Phys.* **12** (2016) 626–629.
8. M. P. Makwana and R. V. Craster, Designing multidirectional energy splitters and topological valley supernetworks, *Phys. Rev. B* **98** (2018) 235125.
9. Z. Gao, Z. Yang, F. Gao, H. Xue, Y. Yang, J. Dong and B. Zhang, Valley surface-wave photonic crystal and its bulk/edge transport, *Phys. Rev. B* **96** (2017) 201402.
10. J.-W. Dong, X.-D. Chen, H. Zhu, Y. Wang and X. Zhang, Valley photonic crystals for control of spin and topology, *Nat. Mater.* **16** (2017) 298–302.
11. Y. Yang, H. Jiang, and Z. H. Hang, Topological valley transport in two-dimensional honeycomb photonic crystals, *Sci. Rep.* **8** (2018) 1–7.
12. Y. Kang, X. Ni, X. Cheng, A. B. Khanikaev and A. Z. Genack, Pseudo-spin–valley coupled edge states in a photonic topological insulator, *Nat. Commun.* **9** (2018) 1–7.
13. X.-D. Chen, F.-L. Shi, H. Liu, J.-C. Lu, W.-M. Deng, J.-Y. Dai, Q. Cheng and J.-W. Dong, Tunable electromagnetic flow control in valley photonic crystal waveguides, *Phys. Rev. Appl.* **10** (2018) 044002.

14. X.-T. He, E.-T. Liang, J.-J. Yuan, H.-Y. Qiu, X.-D. Chen, F.-L. Zhao and J.-W. Dong, A silicon-on-insulator slab for topological valley transport, *Nat. Commun.* **10** (2019) 1–9.
15. J. Lu, C. Qiu, L. Ye, X. Fan, M. Ke, F. Zhang and Z. Liu, Observation of topological valley transport of sound in sonic crystals, *Nat. Phys.* **13** (2016) 369–374.
16. L. Ye, C. Qiu, J. Lu, X. Wen, Y. Shen, M. Ke, F. Zhang and Z. Liu, Observation of acoustic valley vortex states and valley-chirality locked beam splitting, *Phys. Rev. B* **95** (2017) 174106.
17. Z. Zhang, Y. Tian, Y. Cheng, Q. Wei, X. Liu and J. Christensen, Topological acoustic delay line, *Phys. Rev. Appl.* **9** (2018).
18. X. Wu, Y. Meng, J. Tian, Y. Huang, H. Xiang, D. Han and W. Wen, Direct observation of valley-polarized topological edge states in designer surface plasmon crystals, *Nat. Commun.* **8** (2017).
19. F. Gao, H. Xue, Z. Yang, K. Lai, Y. Yu, X. Lin, Y. Chong, G. Shvets and B. Zhang, Topologically protected refraction of robust kink states in valley photonic crystals, *Nat. Phys.* **14** (2018) 140–144.
20. L. Zhang, Y. Yang, M. He, H.-X. Wang, Z. Yang, E. Li, F. Gao, B. Zhang, R. Singh, J.-H. Jiang *et al.*, Valley kink states and topological channel intersections in substrate-integrated photonic circuitry, *Laser Photon. Rev.* **13** (2019) 1900159.
21. B.-Z. Xia, S.-J. Zheng, T.-T. Liu, J.-R. Jiao, N. Chen, H.-Q. Dai, D.-J. Yu and J. Liu, Observation of valleylike edge states of sound at a momentum away from the high-symmetry points, *Phys. Rev. B* **97** (2018) 155124.
22. M. Shalaev, W. Walasik and N. M. Litchinitser, Experimental demonstration of valley-Hall topological photonic crystal at telecommunication wavelengths, *CLEO: QELS_Fundamental Science* (Optical Society of America, California, USA 2018, FM4Q–3).
23. T.-W. Liu and F. Semperlotti, Tunable acoustic valley-Hall edge states in reconfigurable phononic elastic waveguides, *Phys. Rev. Appl.* **9** (2018) 014001.
24. P. Wang, L. Lu and K. Bertoldi, Topological phononic crystals with one-way elastic edge waves, *Phys. Rev. Lett*. **115** (2015) 104302.
25. D. Torrent, D. Mayou and J. Sánchez-Dehesa, Elastic analog of graphene: dirac cones and edge states for flexural waves in thin plates, *Phys. Rev. B* **87** (2013) 115143.
26. S. A. Skirlo, L. Lu and M. Soljačić, Multimode one-way waveguides of large Chern numbers, *Phys. Rev. Lett.* **113** (2014) 113904.
27. Z. Wang, Y. Chong, J. D. Joannopoulos and M. Soljačić, Reflection-free one-way edge modes in a gyromagnetic photonic crystal, *Phys. Rev. Lett.* **100** (2008) 013905.
28. S. Raghu and F. D. M. Haldane, Analogs of quantum-Hall-effect edge states in photonic crystals, *Phys. Rev A*, **78** (2008) 033834.
29. F. Haldane and S. Raghu, Possible realization of directional optical waveguides in photonic crystals with broken time-reversal symmetry, *Phys. Rev. Lett.* **100** (2008) 013904.
30. Y. Poo, R.-x. Wu, Z. Lin, Y. Yang, and C. Chan, Experimental realization of self-guiding unidirectional electromagnetic edge states, *Phys. Rev. Lett.* **106** (2011) 093903.
31. X. Ao, Z. Lin, and C. T. Chan, One-way edge mode in a magneto-optical honeycomb photonic crystal, *Phys. Rev. B* **80** (2009) 033105.
32. F. Zolla, G. Renversez, A. Nicolet, B. Kuhlmey, S. Guenneau and D. Felbacq, *Foundations of Photonic Crystal Fibres* (Imperial College Press, London, UK 2005).

33. J. D. Joannopoulos, S. G. Johnson, J. N. Winn and R. D. Meade, *Photonic Crystals, Molding the Flow of Light*, 2nd edn. (Princeton University Press, Princeton, USA 2008).
34. V. Laude, *Phononic Crystals: Artificial Crystals for Sonic, Acoustic, and Elastic Waves*. (Walter de Gruyter GmbH & Co KG, Berlin, Germany 2015) 26.
35. R. V. Craster and S. Guenneau, *Acoustic Metamaterials* (Springer, Dordrecht, 2016).
36. P. Colomban, The use of metal nanoparticles to produce yellow, red and iridescent colour, from bronze age to present times in lustre pottery and glass: solid state chemistry, spectroscopy and nanostructure, *J. Nano Res.* **8** (2009) 109–132.
37. B. Gralak, S. Enoch *et al.*, Structural colors in nature and butterfly-wing modeling, *Opt. Photon. News* **14** (2003) 38–43.
38. A. Colombi, P. Roux, S. Guenneau, P. Gueguen and R. V. Craster, Forests as a natural seismic metamaterial: Rayleigh wave bandgaps induced by local resonances, *Sci. Rep.* **6** (2016) 1–7.
39. M. Lott, P. Roux, S. Garambois, P. Guéguen and A. Colombi, Evidence of metamaterial physics at the geophysics scale: the metaforet experiment, *Geophys. J. Int.* **220** (2020) 1330–1339.
40. M. P. Makwana and R. V. Craster, Geometrically navigating topological plate modes around gentle and sharp bends, *Phys. Rev. B* **98** (2018) 184105.
41. W. Wang, B. Bonello, B. Djafari-Rouhani and Y. Pennec, Topological valley, pseudospin, and pseudospin-valley protected edge states in symmetric pillared phononic crystals, *Phys. Rev. B* **100** (2019) 140101.
42. R. Wiltshaw, R. V. Craster and M. P. Makwana, Asymptotic approximations for Bloch waves and topological mode steering in a planar array of Neumann scatterers, *Wave Motion* **99** (2020) 102662.
43. S. J. Palmer and V. Giannini, Berry bands and pseudo-spin of topological photonic phases, *Phys. Rev. Res.* **3** (2021) L022013.
44. S. J. Palmer, *Revealing Hidden Topologies in Photonic Crystals* (Imperial College London, London, UK 2021).
45. C.-W. Chen, R. Chaunsali, J. Christensen, G. Theocharis and J. Yang, Corner states in a second-order mechanical topological insulator, *Commun. Mater.* **2** (2021) 1–6.
46. L. Li, B. Li, H.-X. Liu and C.-H. Liang, Locally resonant cavity cell model for electromagnetic band gap structures, *IEEE Trans. Antennas Prop.* **54** (2006) 90–100.
47. R. Porter, Plate arrays as a water wave metamaterial, *33rd International Workshop on Water Waves and Floating Bodies, Guidel-Plages, France* (2018) 1–4.
48. R. V. Craster and S. Guenneau, *World Scientific Handbook of Metamaterials and Plasmonics: Volume 2: Elastic, Acoustic and Seismic Metamaterials* (World Scientific, Singapore 2017) 2.
49. G. Aguzzi, C. Kanellopoulos, R. Wiltshaw, R. V. Craster, E. N. Chatzi and A. Colombi, Octet lattice-based plate for elastic wave control, *Sci. Rep.* **12** (2022) 1–14.
50. A. Colombi, D. Colquitt, P. Roux, S. Guenneau and R. V. Craster, A seismic metamaterial: the resonant metawedge, *Sci. Rep.* **6** (2016) 1–6.
51. A. Colombi, V. Ageeva, R. J. Smith, A. Clare, R. Patel, M. Clark, D. Colquitt, P. Roux, S. Guenneau and R. V. Craster, Enhanced sensing and conversion of ultrasonic Rayleigh waves by elastic metasurfaces, *Sci. Rep.* **7** (2017) 1–9.
52. A. Colombi, R. V. Craster, D. Colquitt, Y. Achaoui, S. Guenneau, P. Roux and M. Rupin, Elastic wave control beyond band-gaps: shaping the flow of waves in plates and half-spaces with subwavelength resonant rods, *Front. Mech. Eng.* **3** (2017) 10.

53. J. M. De Ponti, A. Colombi, R. Ardito, F. Braghin, A. Corigliano and R. V. Craster, Graded elastic metasurface for enhanced energy harvesting, *N. J. Phys.* **22** (2020) 013013.
54. J. M. De Ponti, *Graded Elastic Metamaterials for Energy Harvesting* (Springer, Cham 2021).
55. G. J. Chaplain, J. M. De Ponti, G. Aguzzi, A. Colombi and R. V. Craster, Topological rainbow trapping for elastic energy harvesting in graded Su-Schrieffer-Heeger systems, *Phys. Rev. Appl.* **14** (2020) 054035.
56. Z. Zhang, Y. Gu, H. Long, Y. Cheng, X. Liu and J. Christensen, Subwavelength acoustic valley-Hall topological insulators using soda cans honeycomb lattices, *Research* **2019** (2019) 1–8.
57. R. Chaunsali, C.-W. Chen and J. Yang, Subwavelength and directional control of flexural waves in zone-folding induced topological plates, *Phys. Rev. B* **97** (2018) 054307.
58. ——, Experimental demonstration of topological waveguiding in elastic plates with local resonators, *N. J. Phys.* **20** (2018) 113036.
59. D. Qi, Z. Ren and Z. Qu, Valley-protected topological interface state of the elastic wave: from discrete model to multistable mechanical metamaterials, *J. Sound Vib.* **529** (2022) 116908.
60. W. Fang, C. Han, Y. Chen and Y. Liu, Valley Hall elastic edge states in locally resonant metamaterials, *Materials*, **15** (2022) 1491.
61. S. Yves, R. Fleury, F. Lemoult, M. Fink and G. Lerosey, Topological acoustic polaritons: robust sound manipulation at the subwavelength scale, *N. J. Phys.* **19** (2017) 075003.
62. S. Yves, R. Fleury, T. Berthelot, M. Fink, F. Lemoult and G. Lerosey, Crystalline metamaterials for topological properties at subwavelength scales, *Nat. Commun*. **8** (2017) 1–1017.
63. Q. Zhang, Y. Chen, K. Zhang and G. Hu, Dirac degeneracy and elastic topological valley modes induced by local resonant states, *Phys. Rev. B* **101** (2020) 014101.
64. K. Tang, M. Makwana, R. V. Craster and P. Sebbah, Observations of symmetry-induced topological mode steering in a reconfigurable elastic plate, *Phys. Rev. B*, **102**, 214103, 2020.
65. L. Zhang, Y. Yang, M. He, H.-X. Wang, Z. Yang, E. Li, F. Gao, B. Zhang, R. Singh, J.-H. Jiang and H. Chen, Manipulation of valley-polarized topological kink states in ultrathin substrate-integrated photonic circuitry, arXiv, arXiv:1805.03954v2, 2018, preprint: not peer reviewed.
66. T.-W. Liu and F. Semperlotti, Experimental evidence of robust acoustic valley Hall edge states in a non-resonant topological elastic waveguide, *Phys. Rev. Appl.* **11** (2019) 014040.
67. M. Jung, Z. Fan and G. Shvets, Midinfrared plasmonic valleytronics in metagate-tuned graphene, *Phys. Rev. Lett.* **121** (2018) 086807.
68. M. P. Makwana and G. Chaplain, Tunable three-way topological energy-splitter, *Sci. Rep.* **9** (2019) 18939.
69. M. Proctor, P. A. Huidobro, S. A. Maier, R. V. Craster and M. P. Makwana, Manipulating topological valley modes in plasmonic metasurfaces, *Nanophotonics* **9** (2020) 657–665.
70. M. Makwana, R. Craster and S. Guenneau, Topological beam-splitting in photonic crystals, *Opt. Express* **27** (2019) 16088–16102.
71. K. Aki and P. G. Richards, *Quantitative Seismology*, 2nd edn. (University Science Books, Sansalito, CA 2002) 218–235.
72. D. Xiao, W. Yao and Qian Niu, Valley-contrasting physics in graphene: magnetic moment and topological transport, *Phys. Rev. Lett.* **99** (2007) 236809.
73. Y. Ren, Z. Qiao and Q. Niu, Topological phases in two-dimensional materials: a review, *Rep. Progress Phys.* **79** (2016) 066501.
74. J. R. Schaibley, H. Yu, G. Clark, P. Rivera, J. S. Ross, K. L. Seyler, W. Yao and X. Xu, Valleytronics in 2d materials, *Nat. Rev. Mater.* **1** (2016) 1–15.

75. Y. Ren, X. Deng, Z. Qiao, C. Li, J. Jung, C. Zeng, Z. Zhang and Q. Niu, Single-valley engineering in graphene superlattices, *Phys. Rev. B* **91** (2015) 245415.
76. L. Brillouin, *Wave Propagation in Periodic Structures: Electric Filters and Crystal Lattices* (Dover, New York, USA, 1953).
77. C. Kittel, P. McEuen and P. McEuen, *Introduction to Solid State Physics* (Wiley, New York 1996) 8.
78. D. Colquitt, A. Colombi, R. Craster, P. Roux and S. Guenneau, Seismic metasurfaces: sub-wavelength resonators and Rayleigh wave interaction, *J. Mech. Phys. Solids* **99** (2017) 379–393.
79. G. Carta, D. Colquitt, A. Movchan, N. Movchan and I. Jones, Chiral flexural waves in structured plates directional localisation and control, *J. Mech. Phys. Solids* **137** (2020) 103866.
80. ——, One-way interfacial waves in a flexural plate with chiral double resonators, *Philos. Trans. R. Soc. A* **378** (2020) 20190350.
81. Y. A. Melnikov, Green's function of a thin circular plate with elastically supported edge, *Eng. Anal. Bound. Elem.* **25** (2001) 669–676.
82. S. P. Timoshenko and S. Woinowsky-Krieger, *Theory of Plates and Shells* (McGraw-Hill, New York, USA, 1959).
83. P. A. Martin, *Multiple Scattering: Interaction of Time-Harmonic Waves with N Obstacles*. (Cambridge University Press, Cambridge, UK, 2006) 107.
84. P. Martin, Scattering by rings of vertical cylinders, *Proceedings of 30th International Workshop on Water Waves and Floating Bodies* (2015) 141–144.
85. O. Schnitzer and R. V. Craster, Bloch waves in an arbitrary two-dimensional lattice of subwavelength Dirichlet scatterers, *SIAM J. Appl. Math.* **77** (2017) 119–2135.
86. M. J. Lighthill, *An Introduction to Fourier Analysis and Generalised Functions* (Cambridge University Press, Cambridge, UK, 1958).
87. K. F. Graff, *Wave Motion in Elastic Solids* (Oxford University Press, Oxford, UK, 1975).
88. L. D. Landau and E. Lifshitz, *Theory of Elasticity* (Course of Theoretical Physics, Pergamon Press, Oxford, UK 1989).
89. H. Reißner, Über die unsymmetrische biegung dünner kreisringplatten, *Ingenieur-Archiv* **1** (1929) 72–83.
90. L.-W. Cai and S. A. Hambric, Multiple scattering of flexural waves on thin plates, *J. Vib. Acoust.* **138** (2016) 011009.
91. ——, Movable rigid scatterer model for flexural wave scattering on thin plates, *J. Vib. Acoust.* **138** (2016) 1–10.
92. J. D. Kaplunov, L. Y. Kossovitch and E. Nolde, *Dynamics of Thin Walled Elastic Bodies* (Academic Press, Cambridge, USA 1998).
93. D. J. Mead, Plates with regular stiffening in acoustic media: vibration and radiation, *J. Acoust. Soc. Am.* **88** (1990) 391–401.
94. B. Mace, The vibration of plates on two-dimensionally periodic point supports, *J Sound Vib.* **192** (1996) 629–643.
95. G. Carta, M. Nieves, I. Jones, N. Movchan and A. Movchan, Elastic chiral waveguides with gyro-hinges, *Q. J. Mech. Appl. Math.* **71** (2018) 157–185.
96. J. Achenbach, *Wave Propagation in Elastic Solids* (Elsevier, Amsterdam, Netherlands 2012).
97. J. A. Hudson, *The Excitation and Propagation of Elastic Waves* (Cambridge University Press, Cambridge, UK 1980).

98. I. S. Gradshteyn and I. M. Ryzhik, *Table of Integrals, Series, and Products* (Academic Press, Cambridge, USA 2014).
99. D. Crighton, A. Dowling, J. F. Williams, M. Heckl and F. Leppington, Matched asymptotic expansions applied to acoustics, *Modern Methods in Analytical Acoustics* (Springer, Berlin, Germany 1992) 168–208.
100. E. J. Hinch, *Perturbation Methods* (Cambridge University Press, Cambridge, UK 1991).
101. T. Bridges and P. J. Morris, Differential eigenvalue problems in which the parameter appears nonlinearly, *J. Comput. Phys.* **55** (1984) 437–460.
102. L. L. Foldy, The multiple scattering of waves. I. General theory of isotropic scattering by randomly distributed scatterers, *Phys. Rev.* **67** (1945) 107.
103. P. Wootton, J. Kaplunov, and D. Colquitt, An asymptotic hyperbolic–elliptic model for flexural-seismic metasurfaces, *Proc. R. Soc. A*, **475** (2019) 20190079.
104. J. R. Kissell, S. G. Pantelakis and G. N. Haidemenopoulos, Aluminum and Aluminum Alloys, *Handbook of Advanced Materials* (John Wiley & Sons, Ltd, New Jersey 2004) 321–463.
105. A. S. Alzaidi, J. Kaplunov, L. Prikazchikova, P. Wootton and A. Nikonov, The effect of contact conditions on the performance of flexural seismic metasurfaces, *Zeitschrift für angewandte Mathematik und Physik* **73** (2022) 194.
106. Y. D. Kaplunov and L. Y. Kossovich, Asymptotic model of Rayleigh waves in the far-field zone in an elastic half-plane, in *Doklady Physics*, 49 (Nauka/Interperiodica 2004) 234–236.
107. J. Lu, C. Qiu, M. Ke and Z. Liu, Valley vortex states in sonic crystals, *Phys. Rev. Lett.* **116** (2016) 093901.
108. M. Z. Hasan and C. L. Kane, Colloquium: topological insulators, *Rev. Mod. Phys.* **82** (2010) 3045–3067.
109. W.-Y. He and C. T. Chan, The emergence of Dirac points in photonic crystals with mirror symmetry, *Sci. Rep.* **5** (2015) 1–7.
110. T. Ochiai and M. Onoda, Photonic analog of graphene model and its extension: Dirac cone, symmetry, and edge states, *Phys. Rev. B* **80** (2009) 155103.
111. B. I. Halperin, Quantized Hall conductance, current-carrying edge states, and the existence of extended states in a two-dimensional disordered potential, *Phys. Rev. B* **25** (1982) 2185.
112. X.-G. Wen, Gapless boundary excitations in the quantum Hall states and in the chiral spin states, *Phys. Rev. B* **43** (1991) 11025.
113. T. Ochiai, Photonic realization of the (2+1)-dimensional parity anomaly, *Phys. Rev. B* **86** (2012) 075152.
114. Z. Wang, Y. Chong, J. D. Joannopoulos and M. Soljačić, Observation of unidirectional backscattering-immune topological electromagnetic states, *Nature* **461** (2009) 772–775.
115. S. A. Skirlo, L. Lu, Y. Igarashi, Q. Yan, J. Joannopoulos and M. Soljačić, Experimental observation of large Chern numbers in photonic crystals, *Phys. Rev. Lett.* **115** (2015) 253901.
116. K. L. Tsakmakidis, A. D. Boardman and O. Hess, 'Trapped rainbow' storage of light in metamaterials, *Nature* **450** (2007) 397–401.
117. N. Laforge, R. Wiltshaw, R. V. Craster, V. Laude, J. A. I. Martínez, G. Dupont, S. Guenneau, M. Kadic, and M. P. Makwana, Acoustic topological circuitry in square and rectangular phononic crystals, *Phys. Rev. Appl*. **15** (2021) 054056.
118. T. Ochiai, Broken symmetry and topology in photonic analog of graphene, *Int. J. Mod. Phys. B* **28** (2014) 1441004.
119. T. Yoshida and Y. Hatsugai, Bulk-edge correspondence of classical diffusion phenomena, *Sci. Rep.* **11** (2021) 1–7.

120. Y. Hatsugai, Chern number and edge states in the integer quantum Hall effect, *Phys. Rev. Lett.* **71** (1993) 3697.
121. K. Qian, D. J. Apigo, C. Prodan, Y. Barlas and E. Prodan, Theory and experimental investigation of the quantum valley Hall effect, arXiv, arXiv:1803.08781, 2018, preprint: not peer reviewed.
122. T. Ochiai, Topological properties of bulk and edge states in honeycomb lattice photonic crystals: the case of TE polarization, *J. Phys.* **22** (2010) 225502.
123. ——, Bulk-edge correspondence in open photonic systems, *Waves Random Complex Media* (2021) 1–18.
124. W. Yao, S. A. Yang and Q. Niu, Edge states in graphene: from gapped flat-band to gapless chiral modes, *Phys. Rev. Lett.* **102** (2009) 096801.
125. M. S. Dresselhaus, G. Dresselhaus and A. Jorio, *Group Theory: Application to the Physics of Condensed Matter* (Springer 2008).
126. P. W. Atkins and R. S. Friedman, *Molecular Quantum Mechanics*, Vol. 1 (Oxford University Press 2011).
127. V. Heine, *Group Theory in Quantum Mechanics: An Introduction to Its Present Usage* (Dover Publications 1960).
128. K. Sakoda, *Optical Properties of Photonic Crystals*, Vol. 2 (Springer Science & Business Media 2004) 80.
129. J. O'Neill, Ö. Selsil, R. McPhedran, A. Movchan and N. Movchan, Active cloaking of inclusions for flexural waves in thin elastic plates, *Q. J. Mech. Appl. Math.* **68** (2015) 263–288.
130. P. Humbert, Bessel-integral functions, *Proc. Edinburgh Math. Soc.* **3** (1933) 276–285.
131. F. Olver, *Asymptotics and Special Functions* (CRC Press 1997).
132. M. Abramowitz and I. A. Stegun, *Handbook of Mathematical Functions* Vol. 55 (National Bureau of Standards, Washington 1964).

Appendix A

A. Modelling and continuity conditions for elastic beams attached to the surface of thin plates

Consider Fig. 1, showing a thin plate whose displacement field we denote $\boldsymbol{\mathcal{U}}$. We consider a global Cartesian system such that the x–y plane coincides with the neutral plane of the undeformed plate and consider beams attached to the surface of the plate, the neutral axis of the undeformed beam is aligned with the z axis. Throughout, $\nabla = \mathbf{e}_x \frac{\partial}{\partial x} + \mathbf{e}_y \frac{\partial}{\partial y}$ denotes the in-plane two dimensional gradient. We assume a time-harmonic displacement field of the form

$$\boldsymbol{\mathcal{U}}(\mathbf{x}, z, t) = \boldsymbol{\mathcal{U}}(\mathbf{x}, z) \exp(-i\omega t), \tag{A.1}$$

where $\mathbf{x}$ denotes some in-plane position vector $\mathbf{x} = x\mathbf{e}_x + y\mathbf{e}_y$ and z characterises some out-of-plane position vector $z\mathbf{e}_z$. We define regular and hatted quantities to denote the displacement fields of the plate or beams respectively. We make the classic assumptions of thin plates and beams—see for example Landau and Lifshitz (**88**) or Graff (**87**), where we consider the displacement field of the plate to be of the following form

$$\boldsymbol{\mathcal{U}}(\mathbf{x}, z) = \Big(u(\mathbf{x}) - z\frac{\partial w}{\partial x}\Big)\mathbf{e}_x + \Big(v(\mathbf{x}) - z\frac{\partial w}{\partial y}\Big)\mathbf{e}_y + w(\mathbf{x})\mathbf{e}_z. \tag{A.2}$$

Here, the total displacement field is a superposition of the Kirchhoff–Love thin plate displacement field $w\mathbf{e}_z - z\nabla w$ due to pure bending deformations, and $\mathbf{u}(\mathbf{x}) = u(\mathbf{x})\mathbf{e}_x + v(\mathbf{x})\mathbf{e}_y$ corresponds to purely longitudinal deformations in the plane of the plate. We assume that the plate is sufficiently thin such that the Kirchhoff–Love theory is valid; additionally, deformations in $\mathbf{u}(\mathbf{x})$ are assumed to be uniform in z, and hence result in a plane stress field which does not contribute to plate bending (**88**, **96**). For the beams, we need only consider the time harmonic displacement field along the neutral axis, hence

$$\hat{\boldsymbol{\mathcal{U}}}(z) = \hat{\mathbf{u}}(z) + \hat{\mathbf{w}}(z), \tag{A.3}$$

where $\hat{\mathbf{u}}(z) = \hat{u}(z)\mathbf{e}_x + \hat{v}(z)\mathbf{e}_y$ and $\hat{\mathbf{w}}(z) = \hat{w}(z)\mathbf{e}_z$. We non-dimensionalise quantities by introducing some length scale L as follows

$$\mathbf{x} = L\widetilde{\mathbf{x}}, \quad z = L\widetilde{z}, \quad \boldsymbol{\mathcal{U}} = L\widetilde{\boldsymbol{\mathcal{U}}}, \tag{A.4}$$

similarly for hatted quantities. Dropping tildes, the dimensionless system of equations governing longitudinal and flexural deformations within the beams and plate are given by (**87**, **88**)

$$\left[\nabla^4 - \Omega^2\right]\mathbf{w} = \frac{L^3}{D}P_3(\mathbf{x})\mathbf{e}_z, \tag{A.5}$$

$$\nabla(\nabla\cdot\mathbf{u}) - \frac{\beta^2}{\alpha^2}\nabla\wedge\nabla\wedge\mathbf{u} + \frac{\Omega^2 h^2}{12L^2}\mathbf{u} + \frac{L}{\rho h\alpha^2}\mathbf{P}(\mathbf{x}) = \mathbf{0}, \tag{A.6}$$

$$\left\{\frac{d^2}{dz^2} + \hat{\alpha}^2\Omega^2\right\}\hat{\mathbf{w}} = \mathbf{0}, \tag{A.7}$$

$$\left\{\frac{d^4}{dz^4} - \hat{\beta}^4\Omega^2\right\}\hat{\mathbf{u}} = \mathbf{0}. \tag{A.8}$$

$\mathbf{P}$ and $P_3(\mathbf{x})$ respectively denote all in-plane and out-of-plane external source terms with dimension force per unit area which act on the plate, and we define $\mathbf{w} = w\mathbf{e}_z$. In (A.6), the 2D elastic field is assumed to act under plane stress and hence $\alpha^2 = \frac{4\mu(\lambda+\mu)}{\rho(\lambda+2\mu)} = \frac{E}{\rho(1-\nu^2)}$ and $\beta^2 = \frac{\mu}{\rho} = \frac{1}{2}\frac{E}{\rho(1+\nu)}$. Both rotary inertia (for rotations about $\mathbf{e}_z$) and torsional beam deformations are assumed to be negligible and hence ignored. It is convenient to express $\mathbf{u}$ by means of the following dilational and shear potentials

$$\mathbf{u} = (\nabla + \mathbf{e}_z\frac{\partial}{\partial z})\phi + (\nabla + \mathbf{e}_z\frac{\partial}{\partial z})\wedge\boldsymbol{\psi},$$

where $\phi = \phi(\mathbf{x})$, $\psi = \psi(\mathbf{x})$, and we denote $\boldsymbol{\psi} = \psi\mathbf{e}_z$.

Consider a beam, of length $\hat{\ell}$, whose base is centred and attached to the surface of the plate at $z = \frac{h}{2L}$ and $\mathbf{x} = \mathbf{X}$ (as in Fig. 1). At $z = \hat{\ell} + \frac{h}{2L}$, we apply free end conditions

$$\frac{\partial\hat{\mathbf{w}}}{\partial z}\Big|_{z=\hat{\ell}+\frac{h}{2L}} = \mathbf{0}, \qquad \frac{\partial^2\hat{\mathbf{u}}}{\partial z^2}\Big|_{z=\hat{\ell}+\frac{h}{2L}} = \frac{\partial^3\hat{\mathbf{u}}}{\partial z^3}\Big|_{z=\hat{\ell}+\frac{h}{2L}} = \mathbf{0}. \tag{A.9}$$

To apply continuity of displacement and rotation conditions, where the beam and plate intersect, we introduce unknown plate displacements $\boldsymbol{\mathcal{U}}(\mathbf{x} = \mathbf{X}, z = \frac{h}{2L})$ at the centre of the beam. We require

$$\hat{\boldsymbol{\mathcal{U}}}\Big|_{z=\frac{h}{2L}} = \boldsymbol{\mathcal{U}}(\mathbf{x} = \mathbf{X}, z = \frac{h}{2L}), \quad \text{and} \quad \Big[(\nabla + \mathbf{e}_z\frac{\partial}{\partial z})\wedge\hat{\boldsymbol{\mathcal{U}}}\Big]\Big|_{z=\frac{h}{2L}} = \Big[(\nabla + \mathbf{e}_z\frac{\partial}{\partial z})\wedge\boldsymbol{\mathcal{U}}\Big]\Big|_{\substack{\mathbf{x}=\mathbf{X}\\ z=\frac{h}{2L}}}, \tag{A.10}$$

hence the following conditions must be satisfied

$$\hat{\mathbf{w}}\Big|_{z=\frac{h}{2L}} = \mathbf{w}(\mathbf{X}), \qquad \hat{\mathbf{u}}\Big|_{z=\frac{h}{2L}} = \mathbf{u}(\mathbf{X}) - \frac{h}{2L}\Big[\nabla w\Big]\Big|_{\mathbf{x}=\mathbf{X}}, \qquad \frac{\partial \hat{\mathbf{u}}}{\partial z}\Big|_{z=\frac{h}{2L}} = -2\Big[\nabla w\Big]\Big|_{\mathbf{x}=\mathbf{X}}. \tag{A.11}$$

$$\Big[\nabla \wedge \boldsymbol{u}\Big]\Big|_{\mathbf{x}=\mathbf{X}} = \mathbf{0}. \tag{A.12}$$

Equations (A.7) and (A.8), subject to the boundary conditions (A.9) and (A.11), may be solved in terms of the unknowns $\mathbf{w}(\mathbf{X})$, $\mathbf{u}(\mathbf{X})$ and $\Big[\nabla w\Big]\Big|_{\mathbf{x}=\mathbf{X}}$. From these solutions and the definitions given in (2.5)–(2.7), the forces and moments at the base of the beam can be determined. For example, from (2.6), we can determine the moment arising from the beam due to the most general continuity conditions considered, that is from (A.8) satisfying (A.9) and (A.11)

$$\mathbf{M}(\Omega) = \frac{\hat{E}\hat{I}}{L}\frac{\partial}{\partial z}\Big[\nabla \wedge \hat{\mathbf{u}}\Big]\Big|_{z=\frac{h}{2L}} = \frac{\hat{E}\hat{I}}{L}\Bigg\{\frac{\hat{\beta}^2\Omega\Big[u(\mathbf{X})\mathbf{e}_y - v(\mathbf{X})\mathbf{e}_x\Big]\sin\hat{\beta}\sqrt{\Omega}\hat{\ell}\tanh\hat{\beta}\sqrt{\Omega}\hat{\ell}}{\cos\hat{\beta}\sqrt{\Omega}\hat{\ell} + \operatorname{sech}\hat{\beta}\sqrt{\Omega}\hat{\ell}}$$
$$+\frac{\hat{\beta}\sqrt{\Omega}\Big[\nabla \wedge \mathbf{w}\Big]\Big|_{\mathbf{x}=\mathbf{X}}\Big\{\frac{h}{2L}\hat{\beta}\sqrt{\Omega}\sin\hat{\beta}\sqrt{\Omega}\hat{\ell}\tanh\hat{\beta}\sqrt{\Omega}\hat{\ell} + 2\Big(\sin\hat{\beta}\sqrt{\Omega}\hat{\ell} - \cos\hat{\beta}\sqrt{\Omega}\hat{\ell}\tanh\hat{\beta}\sqrt{\Omega}\hat{\ell}\Big)\Big\}}{\cos\hat{\beta}\sqrt{\Omega}\hat{\ell} + \operatorname{sech}\hat{\beta}\sqrt{\Omega}\hat{\ell}}\Bigg\}. \tag{A.13}$$

For continuity of moments, we require $\mathbf{u}(\mathbf{X}) = \mathbf{0}$. Indeed since (A.13) will be conserved within the plate, in (2.2), and assuming $\mathbf{u}(\mathbf{X}) \neq \mathbf{0}$ (A.13) contradicts both the assumptions of Kirchhoff–Love thin plate theory (bending moments and transverse shear forces are due to pure bending (**87**)) and that $\mathbf{u}(\mathbf{x})$ arises from purely longitudinal deformations which do not result in bending (**88**).

Appendix B

B. Complementary coefficients

The coefficients in (2.17)–(2.19) are simple to determine, since (2.17)–(2.19) must satisfy equations (2.13)–(2.15) we find

$$\begin{pmatrix} A_0 \\ B_0 \end{pmatrix} = \frac{1}{\mathcal{W}[J_0(r\sqrt{\Omega}), J_0(ir\sqrt{\Omega})]}\Bigg\{w(\mathbf{X})\begin{pmatrix} \mathcal{W}[1, J_0(ir\sqrt{\Omega})] \\ \mathcal{W}[J_0(r\sqrt{\Omega}), 1] \end{pmatrix}$$
$$-\frac{iL\mathbf{F}\cdot\mathbf{e}_z}{D8\Omega}\begin{pmatrix} \mathcal{W}[H_0(r\sqrt{\Omega}) - H_0(ir\sqrt{\Omega}), J_0(ir\sqrt{\Omega})] \\ \mathcal{W}[J_0(r\sqrt{\Omega}), H_0(r\sqrt{\Omega}) - H_0(ir\sqrt{\Omega})] \end{pmatrix}\Bigg\}\Bigg|_{r=\epsilon}, \tag{B.1}$$

$$\begin{pmatrix} A_i \\ B_i \end{pmatrix} = -\frac{1}{\mathcal{W}[J_1(r\sqrt{\Omega}), J_1(ir\sqrt{\Omega})]}\Bigg\{\frac{M_i}{D8\sqrt{\Omega}}\begin{pmatrix} \mathcal{W}[\frac{H_1(r\sqrt{\Omega})}{i} - H_1(ir\sqrt{\Omega}), J_1(ir\sqrt{\Omega})] \\ \mathcal{W}[J_1(r\sqrt{\Omega}), \frac{H_1(r\sqrt{\Omega})}{i} - H_1(ir\sqrt{\Omega})] \end{pmatrix}$$
$$+[\nabla \wedge \mathbf{w}]\Big|_{\mathbf{x}=\mathbf{X}}\cdot\mathbf{e}_i\begin{pmatrix} \mathcal{W}[r, J_1(ir\sqrt{\Omega})] \\ \mathcal{W}[J_1(r\sqrt{\Omega}), r] \end{pmatrix}\Bigg\}\Bigg|_{r=\epsilon} \quad \text{for subscript } i = 1, 2. \tag{B.2}$$

$$C = \phi(\mathbf{X}), \tag{B.3}$$

$$D = \psi(\mathbf{X}). \tag{B.4}$$

The coefficients for A_0, B_0, A_i, B_i are found in a similar fashion to O'Neill *et al.* (**129**), by utilising the Wronskian operator $\mathcal{W}[\ \ ]$. Note $\mathbf{C}$ and $\mathbf{D}$ within (2.18) and (2.19) are found in a similar way to (B.1) and

(B.2); however, the contribution arising from the J_1 terms within the potentials can be disregarded at leading order—such a statement would not be true if $\nabla\phi\big|_{\mathbf{x}=\mathbf{X}}$ or $\nabla\wedge\boldsymbol{\psi}\big|_{\mathbf{x}=\mathbf{X}}$ were required. All of the Wronskian terms in (B.1)–(B.2) are evaluated at $r=\epsilon$ and asymptotically expanded treating ϵ as a small parameter, and hence assuming functions have small arguments—within these expansions we have disregarded $\mathcal{O}(\epsilon^2)$ terms.

Appendix C

C. Singular asymptotics of conditionally convergent series

We require the singular asymptotics of several series which diverge in the limit as $r\to 0$. These terms are calculated analytically and expressed through Van der Pol's Bessel-integral function of zero order, $Ji_0(x)$, as defined in Humbert (**130**) where the following behaviour is of importance

$$Ji_0(x)=Ci(x)-\log(2)=\log(\frac{x}{2})+\gamma_E-\frac{x^2}{4}+\mathcal{O}(x^4)\quad\text{as } x\to 0. \tag{C.1}$$

Here, γ_E is the Euler–Mascheroni constant. Utilising the Euler–Maclaurin formula (**131**) it is shown, using the notation as in Fig. C.1

$$\lim_{\substack{r\to 0\\ R\to\infty}}\nabla w_{\text{res}}=\frac{M_p\exp(i\boldsymbol{\kappa}\cdot\mathbf{x})}{4\pi^2 D}\int_R^\infty\int_0^{2\pi}\frac{\cos\theta_G\mathbf{e}_x+\sin\theta_G\mathbf{e}_y}{G}\sin(\theta_G-\theta_M)\exp(i\mathbf{G}\cdot r)\,d\theta_G\,dG+o(1). \tag{C.2}$$

Refer to the appendices of (**42**, **85**) for more details. The integral over θ_G is performed by means of the integral representations of the Bessel functions of integer order (**132**). Integrating over θ_G and then G, it can be shown (C.2) becomes (neglecting $o(1)$ terms)

$$\lim_{\substack{r\to 0\\ R\to\infty}}\mathbf{e}_x\cdot\nabla w_{\text{res}}=-\frac{M_p}{4\pi D}\left\{\sin(2\theta_r-\theta_{M_p})\frac{J_1(Rr)}{Rr}-\sin\theta_m Ji_0(Rr)\right\}\exp(i\boldsymbol{\kappa}\cdot\mathbf{x}), \tag{C.3}$$

$$\lim_{\substack{r\to 0\\ R\to\infty}}\mathbf{e}_y\cdot\nabla w_{\text{res}}=-\frac{M_p}{4\pi D}\left\{\cos\theta_m Ji_0(Rr)-\cos(2\theta_r-\theta_{M_p})\frac{J_1(Rr)}{Rr}\right\}\exp(i\boldsymbol{\kappa}\cdot\mathbf{x}). \tag{C.4}$$

Additionally, setting a and $\mathbf{b}$ as appropriate from Appendix A of (**42**), we find

$$\begin{aligned}\lim_{\substack{r\to 0\\ R\to\infty}} i\alpha^2\phi_{\text{res}}\exp(-i\boldsymbol{\kappa}\cdot\mathbf{X})=\frac{3iL}{\pi\rho\Omega^2h^3}\exp(i\boldsymbol{\kappa}\cdot\mathbf{r})\Big\{&\frac{2\mathbf{e}_r\cdot\mathbf{V}_p}{r}J_0(Rr)-\mathbf{e}_r\cdot\mathbf{V}_p\frac{\Omega^2h^2}{12L^2}rJi_0(Rr)\\ -\frac{J_1(Rr)}{Rr}[2iV_p\kappa\cos(2\theta_r-\theta_\kappa-\theta_{V_p})-&r\frac{\Omega^2h^2}{12L^2}\mathbf{e}_r\cdot\mathbf{V}_p]-2V_p\kappa^2\cos(\theta_{V_p}+2\theta_\kappa-3\theta_r)\frac{J_2(Rr)}{R^2r}\Big\},\end{aligned} \tag{C.5}$$

$$\begin{aligned}\lim_{\substack{r\to 0\\ R\to\infty}}\frac{\alpha^2}{i}\psi_{\text{res}}\exp(-i\boldsymbol{\kappa}\cdot\mathbf{X})=\frac{3iL}{\pi\rho\Omega^2h^3}\exp(i\boldsymbol{\kappa}\cdot\mathbf{r})\Big\{&\frac{2\mathbf{e}_\theta\cdot\mathbf{V}_p}{r}J_0(Rr)-\mathbf{e}_\theta\cdot\mathbf{V}_p\frac{\Omega^2h^2}{12L^2}\frac{\alpha^2}{\beta^2}rJi_0(Rr)\\ +\frac{J_1(Rr)}{Rr}[2iV_p\kappa\sin(2\theta_r-\theta_\kappa-\theta_{V_p})+&r\frac{\Omega^2h^2}{12L^2}\frac{\alpha^2}{\beta^2}\mathbf{e}_\theta\cdot\mathbf{V}_p]-2V_p\kappa^2\sin(\theta_{V_p}+2\theta_\kappa-3\theta_r)\frac{J_2(Rr)}{R^2r}\Big\}.\end{aligned} \tag{C.6}$$

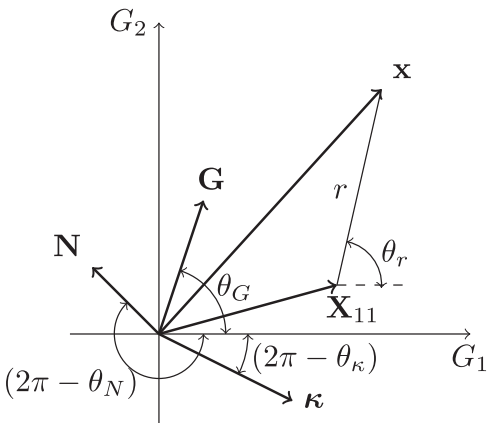

Fig. C.1 The required vector quantities in Fourier space to derive the double sum asymptotics of our Fourier series solutions beyond truncation. Here, **N** refers to either **M** or **V** as appropriate, to be regarded as a constant for some $\boldsymbol{\kappa} = \boldsymbol{\kappa}(\Omega)$ wave of fixed phase.

Expressions (C.5) and (C.6) are differentiated if the associated gradients of potentials are required.

Appendix D

D. The computationally least expensive eigenvalue problem determining dispersion

The polynomial eigenvalue problem in (3.23) can be expressed as a generalised eigenvalue problem by use of the linear companion matrix method (**101**), which further increases the dimension of the system but considers a computationally less expensive eigenvalue problem. The linear companion matrix method can be made even more efficient, provided the matrix multiplying the highest degree term in the polynomial eigenvalue problem is non-singular (**101**). However, our system only contains η^4 terms from (3.9), hence most rows of this matrix will be zero. The inverse of $\mathcal{A}$ is not available and (3.23) cannot be simplified further without another change of variables. By denoting $\gamma = \frac{1}{\eta}$, one can consider

$$\left[\gamma^4\mathcal{E}(\Omega) + \gamma^3\mathcal{D}(\Omega) + \gamma^2\mathcal{C}(\Omega) + \gamma\mathcal{B}(\Omega) + \mathcal{A}(\Omega)\right]\boldsymbol{\Theta} = \mathbf{0}. \tag{D.1}$$

Since (3.9)–(3.11), (3.14), (3.18)–(3.21) all have $\boldsymbol{\kappa}^0$ terms, $\mathcal{E}(\Omega)$ is naturally readily invertible and the generalised eigenvalue problem is further simplified to

$$\left(\widetilde{\mathcal{A}} - \gamma\mathcal{I}\right)\mathbf{Y} = \mathbf{0}, \tag{D.2}$$

where

$$\widetilde{\mathcal{A}} = -\begin{bmatrix} \mathcal{E}^{-1}\mathcal{D} & \mathcal{E}^{-1}\mathcal{C} & \mathcal{E}^{-1}\mathcal{B} & \mathcal{E}^{-1}\mathcal{A} \\ -\mathcal{I} & \mathcal{Z} & \mathcal{Z} & \mathcal{Z} \\ \mathcal{Z} & -\mathcal{I} & \mathcal{Z} & \mathcal{Z} \\ \mathcal{Z} & \mathcal{Z} & -\mathcal{I} & \mathcal{Z} \end{bmatrix}, \qquad \mathbf{Y} = \begin{bmatrix} \gamma^3\boldsymbol{\Theta} \\ \gamma^2\boldsymbol{\Theta} \\ \gamma^1\boldsymbol{\Theta} \\ \boldsymbol{\Theta} \end{bmatrix}. \tag{D.3}$$

Here, $\mathcal{I}$ and $\mathcal{Z}$ respectively denote the identity matrix and a matrix of zeros, both of dimension $(3M + 5P) \times (3M + 5P)$. Finally, one should note $\mathcal{E}$ contains terms from $\mathbf{F}_p$, $\mathbf{M}_p$ and $\mathbf{V}_p$ which will be singular at resonance.

Therefore, approaching resonance $\mathcal{E}$ will be poorly conditioned and hence $\mathcal{E}^{-1}\mathcal{D}$ should be computed with care (similarly for other terms within $\widetilde{\mathcal{A}}$). These products were computed using the minimum norm least-squares solution (MATLAB's lsqminnorm function), which was found to be sufficiently numerically stable for our needs.

Appendix E

E. The external fields

In order to evaluate the unknowns within (4.10)–(4.12), one needs to consider the following approaching the nth scatterer

$$\lim_{\mathbf{x}\to\mathbf{X}_n} w(\mathbf{x}) = w(\mathbf{X}_n) = w_{\text{inc}}(\mathbf{X}_n) + \lim_{\mathbf{x}\to\mathbf{X}_n} \sum_{j=1}^{m} \Big\{ \frac{iL}{8D} F_j w(\mathbf{X}_j) \Big[H_0(r_j\sqrt{\Omega}) - H_0(ir_j\sqrt{\Omega}) \Big] \\ -\mathbf{e}_{\theta\, j} \cdot (\nabla \wedge \mathbf{w})\Big|_{\mathbf{x}=\mathbf{X}_j} \frac{M_j}{8D} \Big[iH_1(r_j\sqrt{\Omega}) + H_1(ir_j\sqrt{\Omega}) \Big] \Big\}, \tag{E.1}$$

$$\lim_{\mathbf{x}\to\mathbf{X}_n} \nabla w(\mathbf{x}) = \nabla w|_{\mathbf{x}=\mathbf{X}_n} = \nabla w_{\text{inc}}(\mathbf{X}_n) + \lim_{\mathbf{x}\to\mathbf{X}_n} \nabla \sum_{j=1}^{m} \Big\{ \frac{iL}{8D} F_j w(\mathbf{X}_j) \Big[H_0(r_j\sqrt{\Omega}) - H_0(ir_j\sqrt{\Omega}) \Big] \\ -\mathbf{e}_{\theta\, j} \cdot (\nabla \wedge \mathbf{w})\Big|_{\mathbf{x}=\mathbf{X}_j} \frac{M_j}{8D} \Big[iH_1(r_j\sqrt{\Omega}) + H_1(ir_j\sqrt{\Omega}) \Big] \Big\}, \tag{E.2}$$

$$\lim_{\mathbf{x}\to\mathbf{X}_n} \phi(\mathbf{x}) = \phi(\mathbf{X}_n) = \phi_{\text{inc}}(\mathbf{X}_n) + \lim_{\mathbf{x}\to\mathbf{X}_n} \sum_{j=1}^{m} \frac{iV_j\sqrt{3}}{2\rho h^2\alpha^2} \mathbf{e}_{r\, j} \cdot \nabla w\Big|_{\mathbf{x}=\mathbf{X}_j} H_1\Big(\frac{\Omega h}{2L\sqrt{3}} r_j\Big), \tag{E.3}$$

$$\lim_{\mathbf{x}\to\mathbf{X}_n} \psi(\mathbf{x}) = \psi(\mathbf{X}_n) = \psi_{\text{inc}}(\mathbf{X}_n) + \lim_{\mathbf{x}\to\mathbf{X}_n} \sum_{j=1}^{m} \frac{V_j\sqrt{3}}{2i\rho h^2\alpha\beta} \mathbf{e}_{\theta\, j} \cdot \nabla w\Big|_{\mathbf{x}=\mathbf{X}_j} H_1\Big(\frac{\alpha}{\beta}\frac{\Omega h}{2L\sqrt{3}} r_j\Big), \tag{E.4}$$

where we denote the $\lim_{\mathbf{x}\to\mathbf{X}_n} r_j = |\mathbf{X}_n - \mathbf{X}_j| = r_{nj}$. The $j = n$th contribution from the above sums, as $r_{nn} \to 0$ for arbitrary angle, introduces logarithmic singularities within (E.2) and $\frac{1}{r_{nn}}$ singularities occurring in (E.3) and (E.4). These singularities are removed by considering the generalised Foldy method, as outlined by Martin (**83**, **84**), by defining the external displacement and potential fields about the nth scatterer as follows

$$w_n(\mathbf{x}) = w(\mathbf{x}) - \Big\{ \frac{iL}{8D} F_n w(\mathbf{X}_n) \Big[H_0(r_n\sqrt{\Omega}) - H_0(ir_n\sqrt{\Omega}) \Big] \\ -\mathbf{e}_{\theta\, n} \cdot (\nabla \wedge \mathbf{w})\Big|_{\mathbf{x}=\mathbf{X}_n} \frac{M_n}{8D} \Big[iH_1(r_n\sqrt{\Omega}) + H_1(ir_n\sqrt{\Omega}) \Big] \Big\}, \tag{E.5}$$

$$\phi_n(\mathbf{x}) = \phi(\mathbf{x}) - \Big\{ \frac{iV_n\sqrt{3}}{2\rho h^2\alpha^2} \mathbf{e}_{r\, n} \cdot \nabla w\Big|_{\mathbf{x}=\mathbf{X}_n} H_1\Big(\frac{\Omega h}{2L\sqrt{3}} r_n\Big) \Big\}, \tag{E.6}$$

$$\psi_n(\mathbf{x}) = \psi(\mathbf{x}) - \Big\{ \frac{V_n\sqrt{3}}{2i\rho h^2\alpha\beta} \mathbf{e}_{\theta\, n} \cdot \nabla w\Big|_{\mathbf{x}=\mathbf{X}_n} H_1\Big(\frac{\alpha}{\beta}\frac{\Omega h}{2L\sqrt{3}} r_n\Big) \Big\}. \tag{E.7}$$